This manuscript of “**Diurnal Warm Layers in the ocean: Energetics, non-dimensional scaling, and parameterization”** is a non-peer reviewed preprint. It has been submitted to Journal of Physical Oceanography.

Diurnal Warm Layers in the ocean: Energetics, non-dimensional scaling, and parameterization

M. Schmitt,[1] H. T. Pham,[2] S. Sarkar,[2,3] K. Klingbeil,[1] L. Umlauf,[1]

[1] *Leibniz-Institute for Baltic Sea Research, Warnemünde, Germany*

[2] *Mechanical and Aerospace Engineering, University of California at San Diego, USA*

[3] *Scripps Institution of Oceanography, University of California at San Diego, USA*

Corresponding author: Mira Schmitt, mira.schmitt@io-warnemuende.de

ABSTRACT: Diurnal Warm Layers (DWLs) form near the surface of the ocean on days with strong solar radiation, weak to moderate winds, and small surface-wave effects. Here, we identify the key non-dimensional parameters for DWL evolution, and use idealized Large Eddy Simulations (LES) and second-moment turbulence modelling, both including the effects of Langmuir turbulence, to study the properties and dynamics of DWLs. We find that the second-moment turbulence models are in excellent agreement with the LES regarding the structure, dynamics, and bulk properties of the DWLs. Comparing tropical and the less frequently studied high-latitude DWLs, we find that rotation at high latitudes strongly modifies the DWL energetics, suppressing net energy turnover and entrainment. Langmuir turbulence has a strong impact on the DWL energy budget in all cases, significantly reduces near-surface shear and stratification, but, for the equilibrium wave fields considered here, only slightly modifies the DWL thickness and other bulk parameters. We find that the scaling relations of Price et al. (1986) provide a reliable representation of the DWL bulk properties at the solar radiation peak across a wide parameter space, including high-latitude DWLs, however, only for a revised set of model coefficients that reflects the effects of Langmuir turbulence and other aspects of our more advanced turbulence model. We identify the timing of the afternoon DWL temperature peak, and provide a description of the DWL bulk parameters also for this characteristic point in the DWL evolution, which may be relevant in many situations.

1. Introduction

Diurnal Warm Layers (DWLs) form near the surface of the ocean on days with strong solar radiation, weak to moderate winds, and weak surface-wave activity. Reviewing existing knowledge, Kawai and Wada (2007) noted that DWLs are a wide-spread feature, found at all latitudes and characterized by typical sea-surface temperature (SST) anomalies of $O(0.1-1)$ °C and typical thicknesses of $O(1-10)$ m. DWLs are relevant to the ocean especially because of their ability to isolate the deeper parts of the surface layer from atmospheric forcing (Wijesekera et al. 2020), provide a niche for marine microorganisms, modify air-sea fluxes (Matthews et al. 2014), and feed back to the atmosphere in ways that are just beginning to be understood (Brilouet et al. 2021).

Recent field investigations with specialized instrumentation (Matthews et al. 2014; Sutherland et al. 2016; Moulin et al. 2018; Hughes et al. 2020a) and numerical modeling studies (Sarkar and Pham 2019; Large and Caron 2015; Bellenger and Duvel 2009) have provided a consistent picture of the physical processes determining the evolution of DWLs in the ocean: strong surface buoyancy forcing tends to suppress near-surface turbulence, separating the deeper parts of the ocean surface layer from direct atmospheric forcing. Analogously, however, the surface buoyancy forcing also induces a trapping of wind-induced momentum, reflected in the evolution of a near-surface diurnal jet with speeds $O(0.1)$ m s^{-1}. The strong shear at the lower edge of the diurnal jet generates a marginally stable stratified shear layer, triggering strong DWL turbulence and entrainment (Hughes et al. 2020a).

This detailed understanding of the DWL dynamics was, however, almost exclusively gained based on investigations at tropical latitudes, despite the observation that during the summer months diurnal SST anomalies at high latitudes may be as large as those found in tropical regions (Kawai and Wada 2007). The few available studies of high-latitude DWLs (e.g., Eastwood et al. 2011; Jia et al. 2023) reported a wide-spread occurrence also in the Arctic Ocean, with DWL temperature anomalies reaching > 5°C during extreme events at latitudes of up to 80°N. Due to the lack of detailed observations and numerical studies of high-latitude DWLs, our understanding of the energetics and parameterization of these features is limited at the moment. Price et al. (1986), e.g., explicitly noted that their frequently used DWL scaling may not be applicable at high latitudes.

A few recent studies focusing on the impact of surface-wave effects on DWLs (Kukulka et al. 2013; Pham et al. 2023; Wang et al. 2023) underlined the importance of Langmuir Turbulence

(LT) for the evolution of diurnal near-surface stratification, typically identifying a reduction of the diurnal SST amplitude and an increase of the DWL thickness due to stronger entrainment. The ability of existing parameterizations (Price et al. 1986) and ocean turbulence models to reproduce these effects has not been systematically evaluated so far.

Here, we attempt to provide a unified description of DWLs in the ocean by first identifying the key non-dimensional parameters that govern their structure and evolution, and then evaluating the influence of these parameters across a large parameter space, including high-latitude and LT effects. Our investigations will be based on a state-of-the art turbulence closure model, validated with the help of Large Eddy Simulations (LES). We will focus on a detailed investigation of the energetics of tropical and high-latitude DWLs, and suggests improved, carefully validated, and widely applicable scaling relations describing the most relevant DWL bulk properties.

2. Model formulation

a. Momentum and buoyancy equations

Our analysis will be based on the one-dimensional transport equations for momentum and buoyancy for an infinitely deep water column,

$$\frac{\partial u}{\partial t} - f(v + v_s) = \frac{\partial}{\partial z}\left(\nu \frac{\partial u}{\partial z}\right) - \frac{\partial \tau_x}{\partial z} \tag{1}$$

$$\frac{\partial v}{\partial t} + f(u + u_s) = \frac{\partial}{\partial z}\left(\nu \frac{\partial v}{\partial z}\right) - \frac{\partial \tau_y}{\partial z} \tag{2}$$

$$\frac{\partial b}{\partial t} = \frac{\partial}{\partial z}\left(\nu^b \frac{\partial b}{\partial z}\right) - \frac{\partial G}{\partial z} + \frac{\partial I_b}{\partial z}\,, \tag{3}$$

where u and v are the Reynolds-averaged velocities in the x- and y-directions, u_s and v_s the corresponding Stokes drift velocities, f the Coriolis parameter, and ν and ν^b the molecular diffusivities of momentum and buoyancy (or heat), respectively. The vertical turbulent momentum fluxes (normalized here with a constant reference density $\rho_0 = 1027$ kg m^{-3}) are denoted by τ_x and τ_y. The evolution of the Reynolds-averaged buoyancy, b, is determined by the vertical turbulent buoyancy flux, G, and the radiative buoyancy flux, I_b, due to penetrating short-wave radiation. We use the conventions that z points vertically upward with $z = 0$ at the surface, that all turbulent fluxes are positive upward, and that the radiative buoyancy flux I_b is positive downward.

The radiative buoyancy flux I_b in (3) is proportional to the downward short-wave radiation,

$$I_b = \frac{\alpha g}{\rho_0 c_p} I \, , \tag{4}$$

where α is the thermal expansion coefficient, g the acceleration of gravity, and c_p the specific heat capacity. The evolution of DWLs is strongly affected by the absorption of short-wave radiation in the near-surface region. For our idealized study focusing on the basic mechanisms of DWL formation, the downward short-wave radiation I will be computed from a simple absorption model of the form

$$I(z) = I_0 \mathrm{e}^{\frac{z}{\eta}} \, , \tag{5}$$

where η is the short-wave absorption scale and I_0 the downward short-wave radiation at the surface.

At the boundaries, the following flux boundary conditions are used for the transport equations in (1)-(3):

$$\nu \frac{\partial u}{\partial z} - \tau_x = \tau_x^0 \quad \text{at} \quad z = 0 \quad , \qquad \frac{\partial u}{\partial z} = 0 \quad \text{at} \quad z = -\infty \tag{6}$$

$$\nu \frac{\partial v}{\partial z} - \tau_y = \tau_y^0 \quad \text{at} \quad z = 0 \quad , \qquad \frac{\partial v}{\partial z} = 0 \quad \text{at} \quad z = -\infty \tag{7}$$

$$\nu^b \frac{\partial b}{\partial z} - G = B_0 \quad \text{at} \quad z = 0 \quad , \qquad \frac{\partial b}{\partial z} = 0 \quad \text{at} \quad z = -\infty \, , \tag{8}$$

where τ_x^0 and τ_y^0 are the components of the surface wind stress (again normalized by ρ_0) and $B_0 = \alpha g Q_{ns} / (\rho_0 c_p)$ the non-solar surface buoyancy flux (positive downward), which is proportional to the non-solar surface heat flux Q_{ns} (accounting for the long-wave, latent, and sensible heat fluxes). Note that Q_{ns} and B_0 will generally be negative (surface heat loss) in our study.

b. Surface forcing

In order to identify the key parameters controlling the DWL evolution and structure, the following analysis will be based on idealized atmospheric fluxes that reflect the essential characteristics of the atmospheric forcing under conditions favorable for DWLs. This forcing consists of a constant non-solar heat (or buoyancy) loss at the surface ($B_0 < 0$), and a periodic diurnal variability induced

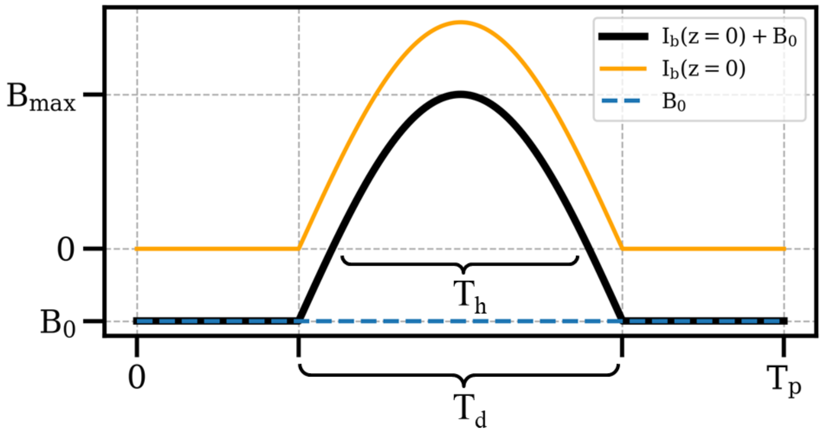

FIG. 1. Idealized buoyancy forcing with the radiative buoyancy flux at the surface, $I_b(z=0)$, the non-solar surface buoyancy flux, B_0, and their sum, the total surface buoyancy flux.

by the radiative heat flux according to

$$I_0(t) = \begin{cases} I_{\max}\cos\left[\frac{\pi}{T_d}(t-\frac{T_p}{2})\right] & \text{for} \quad \frac{T_p}{2}-\frac{T_d}{2} \le t \le \frac{T_p}{2}+\frac{T_d}{2} \\ 0 & \text{for} \quad 0 \le t < \frac{T_p}{2}-\frac{T_d}{2} \quad \text{or} \quad \frac{T_p}{2}+\frac{T_d}{2} < t \le T_p \end{cases} \tag{9}$$

where T_p is the period of the prescribed forcing (24 hours), T_d the daylight period with $I_0 > 0$, and $I_{\max}$ the maximum radiative heat flux reached at $T_p/2$ (midday). The temporal evolution of the surface buoyancy flux B_0, the radiative buoyancy flux at the surface $I_b(z=0)$, computed from I_0 according to (4), and their sum (the total surface buoyancy flux B), are shown in Fig. 1.

The surface buoyancy forcing defined this way is completely described by four dimensional parameters: the two time scales T_p and T_d, the maximum total surface buoyancy flux at midday, $B_{\max}$, and the surface buoyancy loss B_0. Rather than T_d, the more sensible parameter to describe the formation of DWLs is the heating period T_h during which the total surface buoyancy flux B is positive (see Fig. 1). From (9), it is easy to show that these two time scales are related according to

$$T_h = \frac{2T_d}{\pi}\arccos\left(\frac{B_0}{B_0 - B_{\max}}\right) . \tag{10}$$

To reduce the number of free parameters and allow for quasi-periodic solutions, we will assume in many of our simulations that the daily average of the total buoyancy flux is zero, i.e. that the incoming solar radiation is exactly compensated by the net surface buoyancy loss $B_0 T_p$. With this constraint, B_0 and $B_{\max}$ are no longer independent:

$$-\frac{B_{\max}}{B_0} = \frac{\pi}{2}\frac{T_p}{T_d} - 1 \; . \tag{11}$$

In the following, we will often make the additional assumption that $T_d = T_p/2$, which is approximately valid in the tropics and subtropics (and globally around equinox). For this special case, which corresponds to the example shown in Fig. 1, expression (11) yields $B_0 \approx -0.467 B_{\max}$.

Finally, all our simulations will be forced by a constant wind stress in the x-direction, $\tau_x^0 = C_d \frac{\rho_a}{\rho_0} U_{10}^2$, where $\rho_a = 1.23\,\mathrm{kg\,m^{-3}}$ is the air density, U_{10} the 10-meter wind speed, and $C_d = 1.7 \cdot 10^{-3}$ a constant drag coefficient chosen to yield a Langmuir number of $La = 0.3$ (see Section 4b). This introduces the surface friction velocity $u_* = \sqrt{|\tau_x^0|}$ as another key dimensional parameter to the problem.

3. Computation of the turbulent fluxes

The turbulent fluxes of momentum and buoyancy appearing in (1)-(3) will be computed from two different modeling approaches. The first approach will be based on second-moment turbulence modeling, whereas the second approach will use LES, in which the motions providing the most important contributions to the turbulent fluxes τ_x, τ_y, and G are directly resolved.

a. Second-moment turbulence modeling approach

In our second-moment turbulence modeling approach, the turbulent momentum fluxes are computed from down-gradient expressions of the form

$$\tau_x = \langle u'w' \rangle = -\left(\nu_t \frac{\partial u}{\partial z} + \nu_t^S \frac{\partial u_s}{\partial z} \right) \; , \quad \tau_y = \langle v'w' \rangle = -\left(\nu_t \frac{\partial v}{\partial z} + \nu_t^S \frac{\partial v_s}{\partial z} \right) \; , \tag{12}$$

where primes and bracket denotes turbulent fluctuations and ensemble averages, and ν_t and ν_t^S the vertical turbulent diffusivities of momentum related to the Eulerian and Stokes velocities, respectively (Harcourt 2013, 2015). Similarly, the vertical turbulent buoyancy flux is computed from

$$G = \langle w'b' \rangle = -\nu_t^b \frac{\partial b}{\partial z} = -\nu_t^b N^2 \; , \tag{13}$$

with the vertical turbulent diffusivity ν_t^b and the squared buoyancy frequency $N^2 = \partial b/\partial z$.

The turbulent diffusivities ν_t, ν_t^S and ν_t^b are assumed to be related to the turbulent kinetic energy, $k = \overline{u_i' u_i'}/2$, and a turbulence length scale, l, according to

$$\nu_t = c_\mu k^{\frac{1}{2}} l \,, \quad \nu_t^S = c_\mu^S k^{\frac{1}{2}} l \,, \quad \nu_t^b = c_\mu^b k^{\frac{1}{2}} l \,. \tag{14}$$

The stability functions c_μ, c_μ^S and c_μ^b are essential for the representation of the effects of shear and stratification on the anisotropy of turbulence. Our analysis will be based on the stability functions of Harcourt (2015, hereafter H15) that constitute an improved version of an earlier model by Harcourt (2013) and are considered state of the art for the integration of LT effects in second-moment closure models (simplified model versions will be discussed below). Note that the stability functions are presented here using the notation of the Generic Length Scale (GLS) framework (Umlauf and Burchard 2003).

H15 showed that if LT effects are included, c_μ, c_μ^S, and c_μ^b are polynomial functions of the non-dimensional time-scale ratios Nk/ε, Sk/ε, $S_c k/\varepsilon$, and $S_s k/\varepsilon$, where

$$S^2 = \left(\frac{\partial u}{\partial z}\right)^2 + \left(\frac{\partial v}{\partial z}\right)^2 , \quad S_c^2 = \frac{\partial u}{\partial z}\frac{\partial u_s}{\partial z} + \frac{\partial v}{\partial z}\frac{\partial v_s}{\partial z} , \quad S_s^2 = \left(\frac{\partial u_s}{\partial z}\right)^2 + \left(\frac{\partial v_s}{\partial z}\right)^2 , \tag{15}$$

illustrating the direct impact of Stokes shear on the stability functions that was ignored in earlier models of LT (for the exact expressions, see (33) in H15). One example of these earlier models is the one of Kantha and Clayson (2004, KC04 from hereon) that is based on the original stability functions of Kantha and Clayson (1994), ignoring LT effects. The dissipation rate ε follows from the cascading relation

$$\varepsilon = (c_\mu^0)^3 \frac{k^{3/2}}{l} \,, \tag{16}$$

with c_μ^0 denoting the value of c_μ in the logarithmic wall layer (Umlauf and Burchard 2005). The second-moment model is thus closed if the turbulent kinetic energy, k, and the turbulent length scale, l, are known. These parameters are obtained from different types of transport equations as described in detail in Appendix A1.

b. LES modeling approach

The LES approach is used to numerically solve the three-dimensional Craik-Leibovich equations for the grid-filtered Eulerian velocity components, U_i, and buoyancy, B, as follows:

$$\begin{aligned}
\frac{\partial U_i}{\partial x_i} &= 0 \\
\frac{DU_i}{Dt} &= \epsilon_{ijk}(U_j + u_j^s) f_k + \epsilon_{ijk} u_j^s \omega_k - \frac{\partial \Pi}{\partial x_i} + b\delta_{i3} + \nu \frac{\partial^2 U_i}{\partial x_j^2} - \frac{\partial \tau_{ij}^{sgs}}{\partial x_j} \\
\frac{DB}{Dt} &= -u_j^s \frac{\partial B}{\partial x_j} + \nu^b \frac{\partial^2 B}{\partial x_j^2} - \frac{\partial Q_j^{sgs}}{\partial x_j} + \frac{\partial I_b}{\partial z}
\end{aligned} \quad (17)$$

Here, ω_k is the vorticity and $D/Dt = \partial/\partial t + U_j \partial/\partial x_j$. The generalized pressure (Π) is computed as

$$\Pi = \frac{p}{\rho_0} + \frac{2e}{3} + \frac{1}{2}\left[|U_i + u_i^s|^2 - |U_i|^2\right],$$

where p is the dynamic pressure and $e = 1/2\tau_{ii}^{sgs}$ is the subgrid turbulent kinetic energy (TKE). We use the filtered structure function parameterization in Ducros et al. (1996) to compute the subgrid stresses τ_{ij}^{sgs} and a unity subgrid Prandtl number to obtain the subgrid buoyancy flux Q_j^{sgs}. Further details of the numerical method used in the LES can be found in Pham et al. (2023).

The computational domain is a rectangular box with dimensions of 64 × 64 × 72 m in the x, y, and z directions, respectively, using a grid size of 256^3. The grid is uniform in the horizontal (x, y) directions with a spacing of 0.25 m. We use a fine vertical grid spacing of 0.05 m at the surface and mildly stretch the grid at a rate of 3% in the region below.

Periodicity is enforced at the horizontal boundaries. Wind stress τ_x and surface buoyancy flux B_0 are applied at the top surface as implemented in the second-moment turbulence modeling approach. A homogeneous Neumann boundary condition is used at the bottom boundary for the zonal and meridional velocity components, buoyancy and generalized pressure while a Dirichlet boundary condition is used for the vertical velocity component. The LES is initialized with zero velocity and a fixed buoyancy value throughout the domain. Horizontally-averaged profiles of velocities, $\langle U_i \rangle$, buoyancy, $\langle B \rangle$, and turbulent fluxes, $\left\langle U_i' U_j' \right\rangle$, are obtained throughout the simulation and used to compare with the second-moment turbulence model outputs (e.g., u, v, and b) in (1)-(3), as elaborated in Section 5. Here, we use angle brackets to denote horizontal average of the LES fields and primes to denote the fluctuating LES fields from the mean.

4. Non-dimensional description

a. Identification of dimensional parameters

The evolution and physical properties of the DWLs in our idealized simulations are affected by a number of external dimensional parameters, imposed by the atmospheric forcing and the properties of the surface wave field. The former includes the constant wind stress, quantified here with the help of the friction velocity u_* (or, equivalently, the wind speed U_{10}), and the parameters describing the idealized buoyancy forcing shown in Fig. 1: the maximum total buoyancy flux at midday, $B_{\max}$, the (constant) buoyancy loss at the surface B_0, the heating period T_h, and the period of the periodic forcing T_p. Further, the additional length scale η, describing the short-wave penetration depth according to (5), becomes relevant unless the simplifying assumption is made that all radiation is directly absorbed at the surface.

The surface wave field affects the problem primarily through the Stokes drift velocity, u_s, that is assumed to be aligned with the wind speed (and thus $v_s = 0$). This quantity appears in the momentum equations, (1) and (2), the turbulence shear production terms in (A2) and (A3), and some more detailed turbulence modeling assumptions described in Appendix A1. Surface wave properties are represented here by an empirical equilibrium spectrum discussed in Li et al. (2017), as described in Appendix A2. The resulting profile of the Stokes velocity $u_s(z)$, defined in (A14) and (A17), is determined by two dimensional parameters: the surface Stokes velocity, u_s^0, and a vertical decay scale that is determined by the peak wave number k_p (the same two dimensional parameters would also appear for the more simple case of monochromatic waves). Note, however, that in the model of Li et al. (2017) both u_s^0 and k_p depend on the wind speed through (A11) and (A12), and therefore do not constitute fully independent dimensional parameters.

Finally, as all model parameters of the turbulence model are non-dimensional, no additional dimensional parameters are introduced with a single exception. The upper boundary condition for the turbulent length scale l in (A10), or the analogous expression for ω in the $k-\omega$ turbulence model, involves the surface roughness length z_0 that we consider in the following as an additional independent parameter.

TABLE 1. Definition of non-dimensional variables denoted by the ˆ symbol.

$z = \frac{u_*^3}{B_{\max}} \hat{z}$	$t = T_h \hat{t}$	$u, v = u_* \hat{u}, u_* \hat{v}$	$u_s, v_s = u_* \hat{u}_s, u_* \hat{v}_s$	$b = \frac{B_{\max}}{u_*} \hat{b}$	$k = u_*^2 \hat{k}$
$l = \frac{u_*^3}{B_{\max}} \hat{l}$	$\varepsilon = B_{\max} \hat{\varepsilon}$	$\nu_t = \frac{u_*^4}{B_{\max}} \hat{\nu}_t$	$\nu_t^b = \frac{u_*^4}{B_{\max}} \hat{\nu}_t^b$	$I_b = B_{\max} \hat{I}_b$	$f = \frac{\hat{f}}{T_h}$

b. Identification of non-dimensional parameters

The most relevant velocity scale in our problem is the wind speed U_{10} or, equivalently, the friction velocity $u_* = (C_d \rho_a / \rho_0)^{\frac{1}{2}} U_{10}$, which can be used to define the Monin-Obukhov scale, $L_{MO} = u_*^3 / B_{\max}$, as a relevant length scale. If we choose, in addition to these velocity and length scales, the heating period, T_h, as the relevant time scale, we can non-dimensionalize the key variables of our problem (see Tab. 1), and derive non-dimensional versions of the transport equations of momentum and buoyancy in (1)-(3).

From the non-dimensional transport equations, it is straightforward to identify two key non-dimensional parameters of the problem. The first is the non-dimensional Coriolis parameter, $\hat{f} = f T_h = 2\pi T_h / T_f$, which measures the ratio of the heating period and the inertial period, T_f. The second parameter,

$$R = \frac{u_*^2}{T_h B_{\max}} , \tag{18}$$

compares the destabilizing effect of the wind stress, u_*^2, to the stabilizing effect of the total buoyancy supply during the heating period (which is proportional to $T_h B_{\max}$). For simplicity, we ignore the molecular transport terms in (1)-(3) for our dimensional analysis, as their effect is only marginal in our simulations.

Additionally, the buoyancy flux ratio, $B_0 / B_{\max}$, and the timescale ratio, T_h / T_p, appear as independent non-dimensional parameters in our model for the buoyancy forcing. As mentioned in Section 2b above, in many of our simulations, we will use the additional constraint that the daily average of the total net buoyancy flux equals to zero. In this case, combining (10) and (11) yields

$$\frac{T_h}{T_p} = \frac{2}{\pi} \frac{T_d}{T_p} \arccos\left(\frac{2}{\pi} \frac{T_d}{T_p} \right) , \tag{19}$$

revealing a direct one-to-one relation between the timescale ratios T_h / T_p and T_d / T_p. For the tropical value of the daylight ratio, $T_d / T_p = 0.5$, we find $B_0 / B_{\max} = -0.467$ and $T_h / T_p = 0.4$ from

(11) and (19), respectively, suggesting that the heating period can be substantially smaller than the daylight period. The final non-dimensional parameter associated with the buoyancy forcing is the non-dimensional decay length scale, $\hat{\eta} = \eta / L_{MO}$, introduced via the simple light absorption model in (5). Assuming that all short-wave radiation is absorbed at the surface, as in many of the examples studied below, the dependence on this non-dimensional parameter vanishes.

Finally, if the non-dimensional Stokes velocity $\hat{u}_s = u_s / u_*$ is computed from (A17), the Langmuir number $\mathrm{La} = (u_*/u_s^0)^{\frac{1}{2}}$ and the non-dimensional peak wave number $\hat{k}_p = k_p L_{\mathrm{MO}}$ appear in (A14) as additional non-dimensional products characterizing the surface wave forcing. However, from the quadratic drag law, $u_*^2 = C_d(\rho_a/\rho_0)U_{10}^2$, and the expression for the surface Stokes drift in (A11), we find $\mathrm{La} = (\rho_a C_d)^{\frac{1}{4}} / (\rho_0 c_s^2)^{\frac{1}{4}} \approx 0.3$, suggesting that La is fixed at a value typical for an equilibrium wave field. Similarly, it can be shown from (A11) and (A12) that $\hat{k}_p \propto g u_* / B_{\max}$, suggesting $g u_* / B_{\max}$ as an additional non-dimensional parameter that can be interpreted as the ratio of L_{MO} and the peak wave length, or, equivalently, the vertical Stokes decay scale. However, it turns out that the effect of this parameter is difficult to study independently in practice. At a fixed g, and keeping other parameters like R and $\hat{f}$ constant, it is easy to show that $\hat{k}_p$ can only be varied by changing $u_*/B_{\max}$ while keeping $u_*^2/B_{\max} \propto R$ constant. This is possible only over a very restricted parameter range if the non-dimensional solutions are to represent a physically relevant situation (see below).

As mentioned above, the only dimensional parameter arising from the turbulence model is the surface roughness length, z_0, that transforms into the non-dimensional roughness parameter $\hat{z}_0 = z_0 / L_{\mathrm{MO}}$. Physically, z_0 represents the length scale of turbulence at the surface. This parameter is not well constrained but, as shown below, many of our results turned out to be insensitive with respect to changes in $\hat{z}_0$.

All non-dimensional parameters present in this study are summarized in Table 2. We carefully checked that different numerical solutions indeed collapse if all non-dimensional parameters are kept constant and all variables are non-dimensionalized as in Tab. 1.

5. Model validation

To evaluate the performance of the different second-moment closure models used in our study, we compare them to our LES results for some typical DWL scenarios. Both types of models are

TABLE 2. The non-dimensional parameters. Note that the variability of some parameters appearing in brackets is restricted on our model.

$R = \frac{u_*^2}{T_h B_{\max}}$	$\hat{f} = f T_h$	$\frac{T_h}{T_p}$	$\frac{B_0}{B_{\max}}$
$\hat{z}_0 = \frac{z_0}{L_{MO}}$	$\hat{\eta} = \frac{\eta}{L_{MO}}$	$(\mathrm{La} = 0.3)$	$\left(\hat{k}_p \propto \frac{g u_*}{B_{\max}}\right)$

driven with identical atmospheric and buoyancy forcing and use the same parametric surface-wave model, described in Appendix A2, to compute the Stokes velocities.

The three different versions of the second-moment models, described in detail in Section 3 and Appendix A1, are: (a) the full model of H15, which represents LT effects in both the stability functions and the transport equations for k and kl through the additional Stokes production term P_s in (A1) and (A4), respectively; (b) the model of KC04, which only considers the additional Stokes production terms in the transport equations but ignores the impact of LT on the stability functions; and (c) the model of Kantha and Clayson (1994), which ignores LT effects entirely. Recall that the models of H15 and KC04 converge to the model of Kantha and Clayson (1994) for the special case of zero Stokes drift ($u_s = 0$), which allows for a clear separation of LT effects from other modeling components. To compute the turbulent length scale l, we used an extended version of the Mellor-Yamada equation for kl for all of the following simulations but we will also include a short comparison with a modified version of the k-ω model in the supplementary material (see detailed description in Appendix A1).

All second-order moment model runs were conducted with a modified version of the General Ocean Turbulence Model (GOTM), described in detail in Umlauf et al. (2005). The time step for these simulations was set to 6 s, and a 50 m deep water column was resolved with 500 grid cells with a resolution of 0.015 m at the surface, gradually decreasing towards the bottom. These parameters were found to ensure numerical convergence and exclude any impact of the lower edge of the domain on the DWL properties.

For all these simulations, we use a peak solar heat flux of $I_{\max} = 400$ W m^{-2} at noon, and assume, for simplicity, that the non-solar heat flux vanishes ($B_0 = 0$) and that all short wave radiation is absorbed at the surface ($\eta = 0$). The heating period is $T_h = T_d = 12$ h at a tropical latitude of 10°N (corresponding to $f = 2.53 \cdot 10^{-5}$ s^{-1} and a local inertial period of $T_f = 69.1$ h). A constant wind stress of $\tau_x^0 = 2 \cdot 10^{-5}$ m^2 s^{-2} ($u_* = 4.4 \cdot 10^{-3}$ m s^{-1}) is applied, equivalent to a wind speed of

$U_{10} = 3.1$ m s^{-1} (light breeze) for the constant C_d mentioned above (in all our simulations $\tau_y^0 = 0$). To save computational resources for the LES, the simulations start at 05:00 in the morning (one hour before the start of the buoyancy forcing) rather than at midnight. The second-moment model starts at midnight, but, for better comparison with the LES, the wind was not turned on until 05:00 in the morning. Note that in all the other sections, the wind starts at the beginning of the simulations, i.e at midnight.

The horizontally averaged LES results are shown in Fig. 2, comparing simulations without ($u_s = 0$) and with LT. In both cases, the buoyancy structure (Fig. 2a,b) shows the evolution of DWLs with similar characteristics. LT effects are clearly noticeable only in the reduced near-surface buoyancy in the simulation with wave forcing, which is consistent with the reduced near-surface stratification due to LT-enhanced mixing (Fig. 2c,d). The Eulerian shear (Fig. 2c,d) in the simulation with LT deviates from its counterpart with $u_s = 0$ significantly in the upper 2 m, where the Stokes shear production P_s becomes the dominant source of turbulence (u_s decays to approximately 10% of its surface value within the uppermost 0.65 m). This effect is also clearly evident in the Richardson number, $Ri = N^2 S^{-2}$, which ignores the Stokes shear (Fig. 2e,f).

Figs. 3 and 4 compare the DWL evolution in the LES (with and without LT) and the second-moment models for four selected points in time (marked in Fig. 2). This comparison shows that the overall characteristics of the LES are reproduced well by all models: both the DWL thicknesses and the vertical structures of buoyancy, velocity, and the turbulent momentum flux closely correspond to those predicted by the LES. Significant differences are largely confined to the upper 1-2 m, where the LES suggest a strong reduction of stratification and shear due to the effects of LT. For the period between 12:00 and 15:00, when DWL anomalies are most distinct, the inlay plots in Fig. 3d,f show that the inclusion of LT effects leads to a significant reduction of the near-surface shear. The velocity structure in this region is in close agreement with the LES only for H15, while the model of KC04 clearly underestimates the additional mixing of momentum due to LT effects, underlining the importance of the Stokes shear term in (12). For the near-surface buoyancy profiles (see inlay plots in Fig. 3c,e), differences between the models are less pronounced, and all tend to underestimate the reduction of near-surface stratification due to LT. Differences between the simulations with and without LT become especially clear in the gradient Richardson number

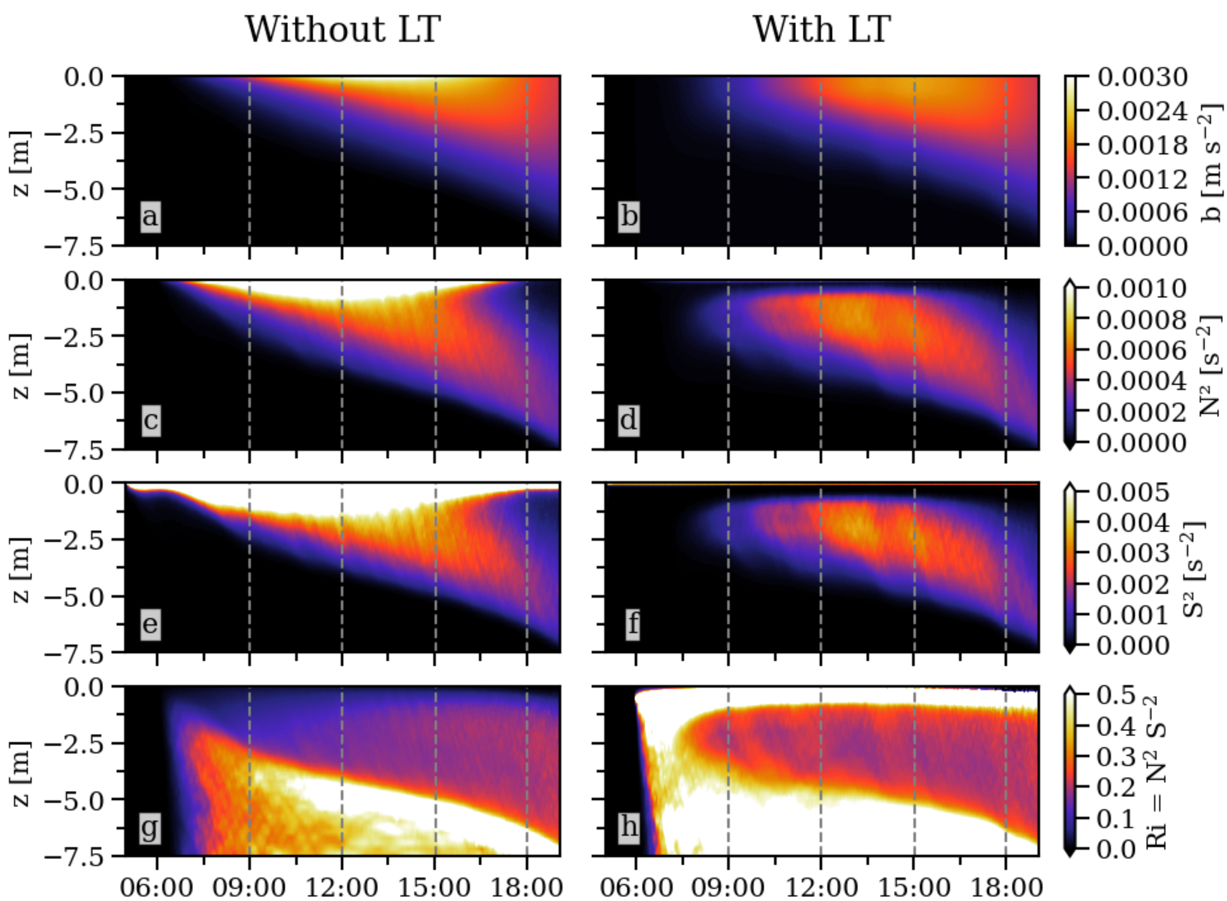

FIG. 2. Evolution of (a,b) buoyancy, (c,d) buoyancy frequency squared, (e,f) total Eulerian shear squared, and (g,h) gradient Richardson number for a typical DWL scenario without (left) and with LT forcing, respectively. Shown are horizontally averaged LES results for the forcing parameters discussed in Section 5. Dashed vertical lines mark the profiles shown in Figs. 3 and 4.

shown in Fig. 4b,d,f,h. The strong near-surface peak of *Ri* is reflected only by the model of H15 for the entire evolution of the DWL.

It is worth noting that all second-moment models predict virtually identical profiles underneath the thin near-surface region directly affected by Stokes production. For the LES, this is the case only for the late-stage DWLs (Fig. 3e-g), while the DWL evolution in the morning and around noon (Fig. 3a-d) shows weak but significant deviations also below the Stokes layer. This points at a non-local energy transfer from the Stokes layer towards the deeper regions of the DWL, which is not represented in the second-moment models.

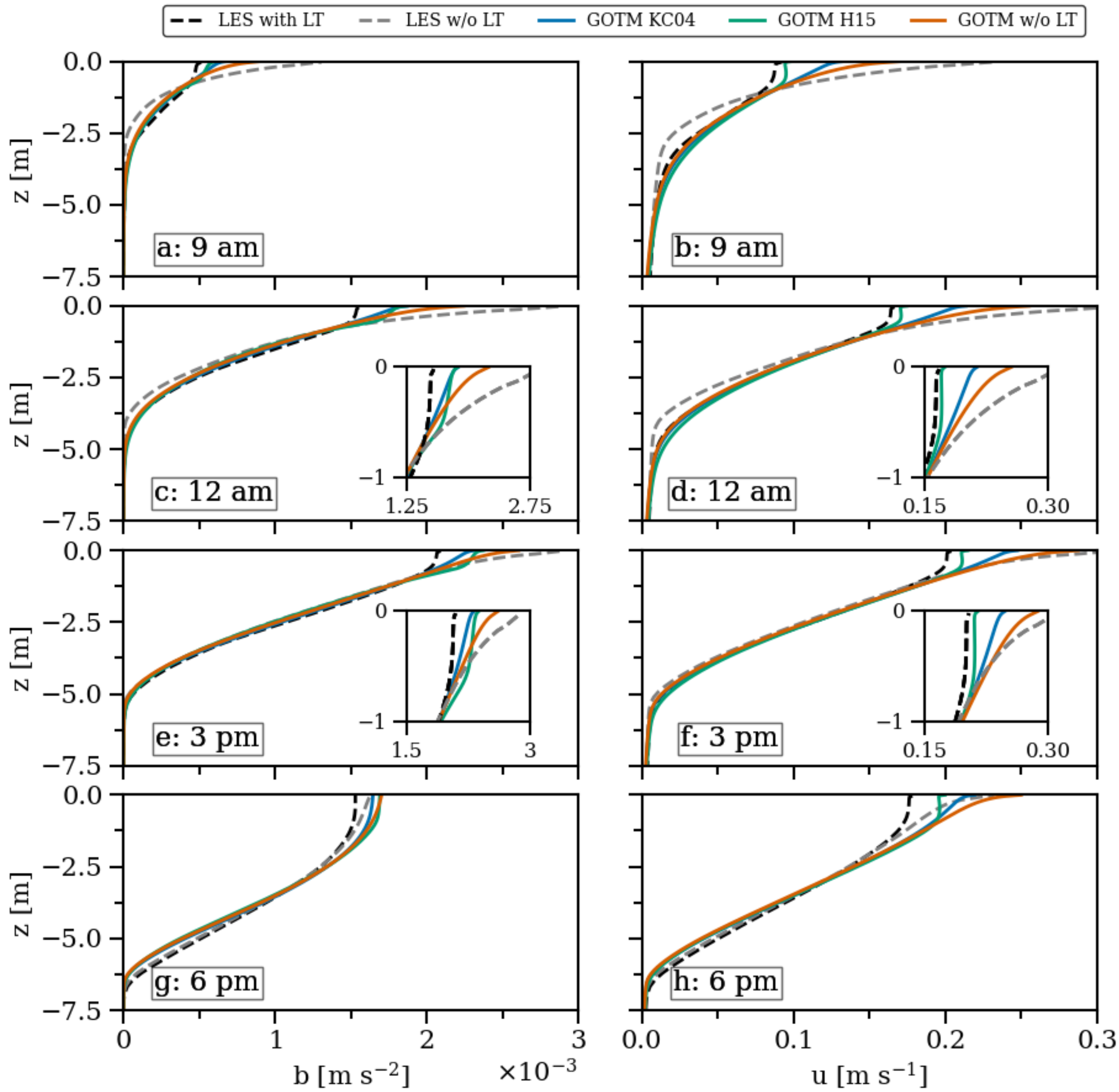

FIG. 3. Comparison of LES and GOTM simulations for (a,c,e,g) buoyancy and (b,d,f,h) u-component of the velocity at the times indicated in Fig. 2. Dashed lines show LES results with (black) and without (gray) LT. Colored lines correspond to different second-moment models as indicated in the legend. Inlays panels in (c-f) show enlarged views of the near-surface region.

Overall, we conclude that the performance of the model of H15 is most satisfying, and we will therefore use this model for most of the following numerical investigations. As shown in the supplementary material, simulations conducted with a modified version of the k-ω model (see

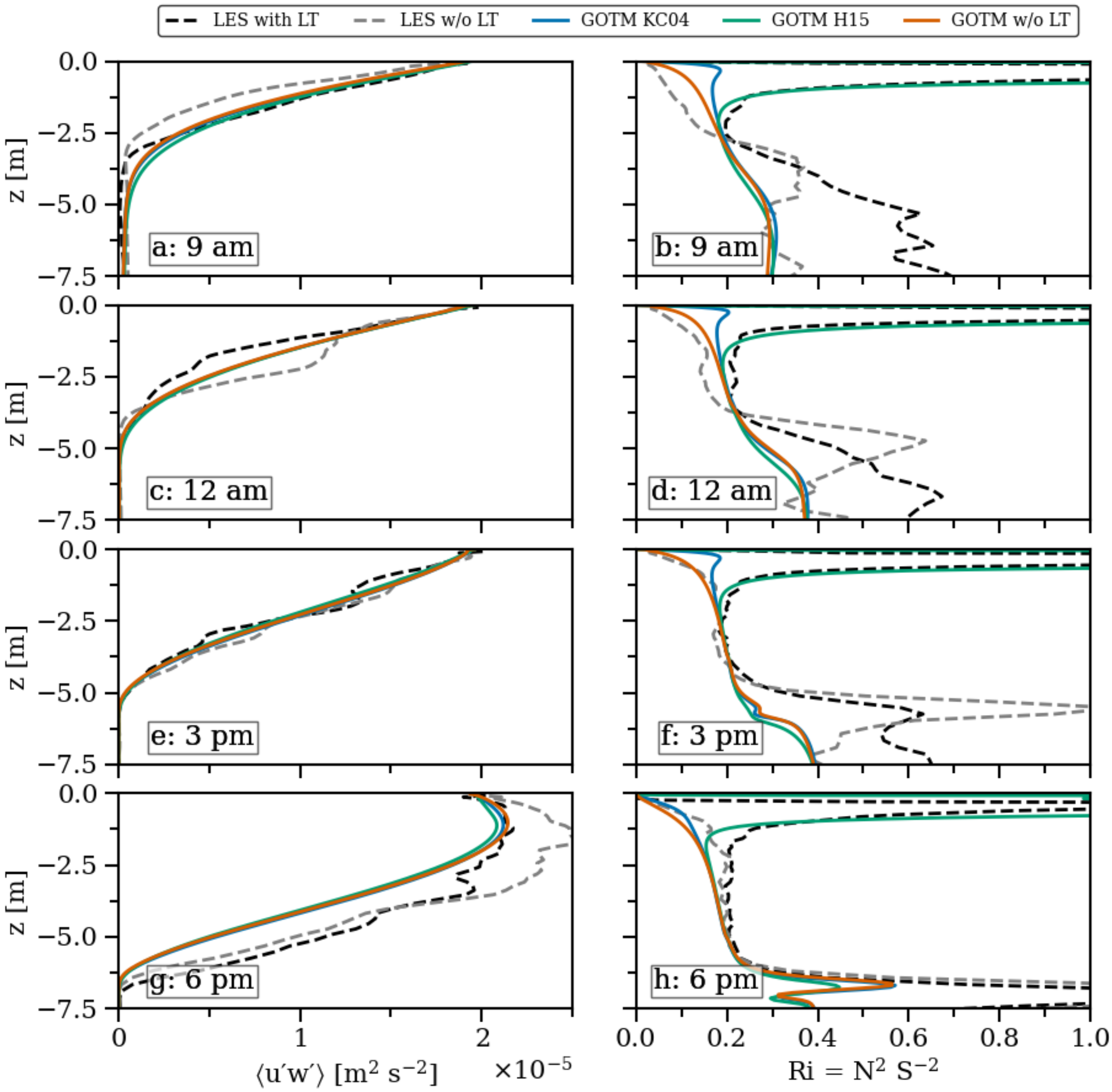

FIG. 4. As in Fig. 3 but now for (a,c,e,g) total (resolved plus subgrid-scale) turbulent momentum flux $\langle u'w' \rangle$ and (b,d,f,h) gradient Richardson number Ri.

Appendix A1), using the same stability functions of H15, yields very similar results, providing some support for the robustness of our results.

6. DWL energetics

a. Theory

For the analysis of the DWL energetics, it is convenient to define a DWL-averaged buoyancy, $\overline{b}$, and a DWL thickness, h, based on expressions of the form

$$\overline{b}h = \int_{z_{\mathrm{ref}}}^{0} \tilde{b}\,\mathrm{d}z\,, \quad \varphi\overline{b}h^2 = -\int_{z_{\mathrm{ref}}}^{0} \tilde{b}z\,\mathrm{d}z\,. \tag{20}$$

where $\tilde{b} = b - b_{\mathrm{ref}}$ is the DWL buoyancy anomaly, referenced with respect to the buoyancy b_{ref} at some reference level z_{ref} below the DWL, and φ a shape factor that depends on the vertical structure of the buoyancy profile. E.g., it can be shown that $\varphi = 1/2$ and $\varphi = 1/3$ correspond to the cases of well-mixed and linearly stratified DWLs, respectively. Reformulating (3) in terms of $\tilde{b}$, ignoring the molecular fluxes, and integrating the resulting equation vertically between z_{ref} and the surface, the time derivative of the first relation in (20) can be expressed as

$$\frac{\mathrm{d}(\overline{b}h)}{\mathrm{d}t} = \frac{\mathrm{d}}{\mathrm{d}t}\int_{z_{\mathrm{ref}}}^{0} \tilde{b}\,\mathrm{d}z = B_0 + I_b^0 + \dot{b}_{\mathrm{ref}} z_{\mathrm{ref}} \tag{21}$$

which reflects the heat budget of the DWL, expressed in terms of buoyancy. The last term in (21) accounts for the temporal change in the reference buoyancy. While this term may be relevant in observations or more complex numerical modeling studies, in our idealized simulations this term becomes negligible shortly after the DWL has formed, and will therefore be ignored in the following.

The second expression in (20) is recognized as the potential energy anomaly, E_{pot}, induced by the presence of the DWL. Reformulating (3) in terms of $\tilde{b}$, multiplying the result by z, and integrating by parts, yields an equation for the evolution of the potential energy anomaly:

$$\frac{\mathrm{d}}{\mathrm{d}t}E_{\mathrm{pot}} = \frac{\mathrm{d}(\varphi\overline{b}h^2)}{\mathrm{d}t} = -\frac{\mathrm{d}}{\mathrm{d}t}\int_{z_{\mathrm{ref}}}^{0} \tilde{b}z\,\mathrm{d}z = -\int_{z_{\mathrm{ref}}}^{0} G\,\mathrm{d}z - h\overline{I}_b - \frac{1}{2}\dot{b}_{\mathrm{ref}} z_{\mathrm{ref}}^2\,, \tag{22}$$

where we again ignored the molecular fluxes and introduced $\overline{I}_b = h^{-1} \int_{z_{\mathrm{ref}}}^{0} I_b \mathrm{d}z$. In the derivation of (22), we have assumed $I_b(z_{\mathrm{ref}}) \ll I_b^0$ to insure that our analysis includes the entire near-surface region with significant radiative heating. Similar to (21), the final term in (22), involving the time derivative of b_{ref}, is found to be negligible in our simulations, and will henceforth be ignored.

Using (21), the energy budget in (22) can thus be re-arranged in the form

$$\underbrace{\varphi h \left(B_0 + I_b^0 + \frac{\overline{I}_b}{\varphi}\right)}_{\substack{\text{work required to}\\ \text{mix down buoyancy}\\ \text{added near surface}}} + \underbrace{\varphi h \overline{b} w_e}_{\substack{\text{work required}\\ \text{to mix up}\\ \text{entrained fluid}}} + \underbrace{\dot{\varphi} \overline{b} h^2}_{\substack{\text{work required to}\\ \text{change the DWL}\\ \text{buoyancy structure}}} = \underbrace{-\int_{z_{\mathrm{ref}}}^{0} G \mathrm{d}z}_{\substack{\text{work done}\\ \text{by turbulence}}} , \tag{23}$$

where we introduced the entrainment velocity $w_e = \dot{h}$. The energy budget in (23) states that the work performed by turbulence against gravity (right hand side) is used to: (a) mix down buoyancy deposited at or near the surface by the atmospheric and radiative heat fluxes, (b) mix up fluid entrained at the bottom of the DWL, and (c) change the shape of the buoyancy profile inside the DWL. The relative importance of these terms will be investigated in more detail below.

Similarly, an equation for the DWL kinetic energy can be obtained by multiplying the momentum equations in (1) and (2) with u and v, respectively, adding the results, and integrating from z_{ref} to the surface. Ignoring again the molecular flux terms for simplicity, this yields an energy budget of the form:

$$\frac{\mathrm{d}}{\mathrm{d}t} E_k = \frac{\mathrm{d}}{\mathrm{d}t} \int_{z_{\mathrm{ref}}}^{0} \frac{u^2 + v^2}{2} \mathrm{d}z = \mathbf{u}^0 \cdot \boldsymbol{\tau}^0 + \int_{z_{\mathrm{ref}}}^{0} f \mathbf{k} \cdot (\mathbf{u} \times \mathbf{u}_s) \, \mathrm{d}z - \int_{z_{\mathrm{ref}}}^{0} P \mathrm{d}z + z_{\mathrm{ref}} \frac{\mathrm{d}}{\mathrm{d}t} \left[\frac{u_{\mathrm{ref}}^2 + v_{\mathrm{ref}}^2}{2} \right] , \tag{24}$$

where $\mathbf{k}$ is the upward unit vector and $\mathbf{u}^0$ the velocity at the surface. The terms on the right hand side of (24) can be interpreted as: (a) the work performed by the wind stress on the DWL, (b) the exchange of kinetic energy with the surface wave field due to the effect of rotation (see, e.g., Suzuki and Fox-Kemper 2016), and (c) the loss of kinetic energy to TKE by turbulence shear production. The final term on the right hand side of (24), representing the change in the reference kinetic energy relative to which the DWL kinetic energy is measured, is again negligible in our simulations.

The shear production term in (24) connects the DWL kinetic energy to the vertically integrated TKE equation,

$$-\int_{z_{\mathrm{ref}}}^{0} G \mathrm{d}z = -\int_{z_{\mathrm{ref}}}^{0} \dot{k} \mathrm{d}z + \int_{z_{\mathrm{ref}}}^{0} (P + P_s) \mathrm{d}z - \int_{z_{\mathrm{ref}}}^{0} \varepsilon \mathrm{d}z \,, \tag{25}$$

which is easily derived from (A1). The left hand side of (25) and the right hand side of the potential energy budget in (23) are identical, showing that the energy required for mixing within the DWL corresponds to the fraction of the (mean flow and Stokes) shear production that is neither dissipated nor used to change the DWL integrated TKE. The relative importance of the various terms in the DWL energy budgets in (23), (24), and (25) will be investigated in the following discussion.

b. Results

To investigate the DWL energy budgets derived above, we compare a typical tropical case at 10°N with a high-latitude DWL at 70°N (T_f = 12.6 h), focusing especially on the effects of rotation and day length for high-latitude DWLs that have so far received only little attention. For both cases, we assume typical midsummer values for the peak radiative heat flux, I_{max}, corresponding to the different latitudes, respectively (Tab. 3). For the tropical case, as before, the period with non-zero solar radiation was chosen as T_d = 12 h (between 6:00 h and 18:00 h), whereas we assume T_d = 18 h (between 3:00 h and 21:00 h) for the high-latitude case. These values yielded an acceptable agreement between our simplified solar radiation model in (9) and the realistic variations of the short wave radiation around midsummer. Numerical tests with a more realistic expression showed only small differences in the DWL evolution that did not affect any of the conclusions drawn in the following. Finally, as shown in Fig. 1, we assume that the surface buoyancy loss B_0 due to cooling at the surface exactly compensates the radiative buoyancy supply over the course of a day, implying that B_0 and the maximum net buoyancy flux at noon, B_{max}, are related according to (11). Tab. 3 shows that the equivalent surface heat loss Q_{ns} (or, equivalently, the surface buoyancy loss B_0) are comparable in the two cases, implying that also the integrated (in time) radiative heat fluxes are similar. With these assumptions, the effective heating periods T_h = 9.5 h and T_h = 12.2 h follow from (19) for the tropical and high-latitude case, respectively.

To highlight the role of high-latitude effects, the parameters in Tab. 3 were chosen to yield identical values for the key non-dimensional products that do not include any direct latitudinal

TABLE 3. Atmospheric forcing and non-dimensional parameters used for the analysis of the DWL energetics. Note that $R = 0.0015$ and $\hat{z}_0 = 0.01$ are identical for both simulations.

	I_{max} [W m^{-2}]	Q_{ns} [W m^{-2}]	U_{10} [m s^{-1}]	$T_h/T_f = \hat{f}/(2\pi)$	T_h/T_p	B_0/B_{max}	$\hat{k}_p$
10°N	1050	-334	4	0.14	0.4	-0.47	0.16
70°N	680	-325	3.2	0.97	0.51	-0.91	0.26

dependency: $R = u_*^2/(B_{max}T_h) = 0.0015$ and $\hat{z}_0 = 0.01$. As in the previous chapter, all short wave radiation is assumed to be absorbed at the surface ($\hat{\eta} = 0$). The main differences for the high-latitude case, in non-dimensional terms, are thus the much larger - by a factor of 7 - value of the non-dimensional Coriolis parameter $\hat{f} \propto T_h/T_f$, the larger time scale ratio T_h/T_p due to the larger day length at high latitudes, and, indirectly, the larger non-dimensional peak wave number $\hat{k}_p$ due to the smaller B_{max}. Both simulations started at midnight ($t/T_f = 0$) and were run for $T_p = 24$ h with the parameters compiled in Tab. 3, using the same numerical grid and time step as in Section 5.

The evolution of the near-surface buoyancy for the two cases is shown in Figs. 5a and 6a. The DWL thickness, h, as one of the most important bulk parameters, is defined here by a simple density threshold, identifying the lower edge of the DWL with the vertical position where the buoyancy has decayed to 5% of its maximum value. Figs. 5a and 6a show that this definition provides a plausible representation of the vertical extent of the DWL for the two cases summarized in Tab. 3. It is worth noting that the following alternative approach to define the DWL thickness, based on the DWL potential energy, yields very similar results, suggesting that our estimates for the DWL thickness as $h(5\%)$ are robust. In this approach, the DWL thickness is computed from the ratio of the integrals in (20), assuming a constant shape factor of $\varphi = 1/3$. This value of φ corresponds to a linearly stratified DWL, as typically observed in our simulations (see, e.g., Fig. 3). Note from (20) that this integral-based approach connects changes in h to changes in the vertical position of the DWL center of mass due to mixing, and therefore has a clear energetic interpretation.

Figs. 5a and 6a show that both definitions yield consistent DWL thicknesses for the core period between the DWL formation in the morning until approximately 15:00 in the afternoon. In the later afternoon and evening, (20) tends to overestimate the DWL thickness as the shape factor φ tends to be larger than $\varphi = 1/3$ for the more well-mixed DWLs observed during this period (see

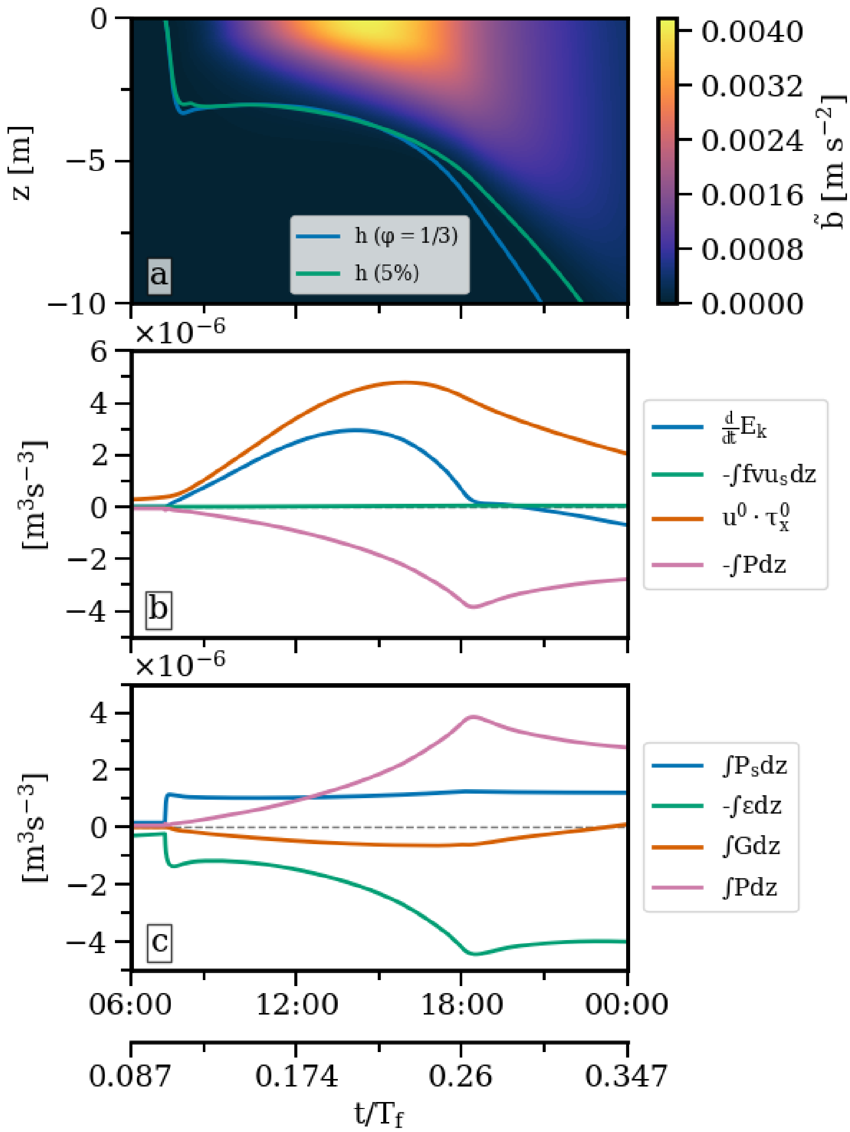

FIG. 5. Evolution of (a) DWL buoyancy anomaly, (b) DWL kinetic energy budget in (24), and (c) turbulent kinetic energy budget in (25) for the equatorial case at 10°N (Tab. 3). Colored lines in (a) show the DWL thickness h computed from the ratio of the integrals in (20) with a constant $\varphi = 1/3$ (blue) and the depth at which the buoyancy has dropped to 5% of its maximum value (green). Note that the simulation starts at midnight ($t/T_f = 0$), and that both the wind stress and Stokes drift point into the x-direction ($\tau_y^0 = 0$ and $v_s = 0$).

Fig. 7b below). The following analysis will therefore be based on the 5% buoyancy threshold. The reference level z_{ref} is chosen to coincide with the location of the minimum buoyancy in the water column, and $\tilde{b} = b - b_{\text{ref}}$ is defined based on the reference buoyancy b_{ref} found at this depth. This

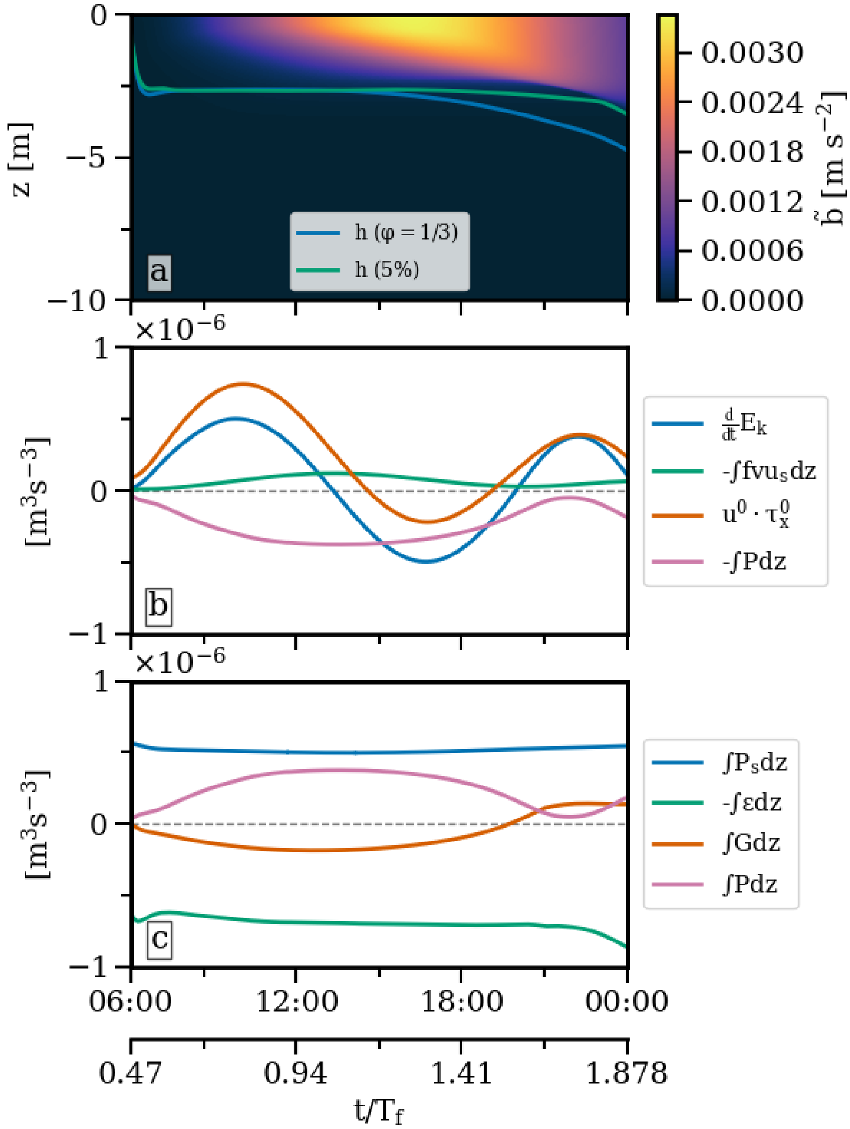

FIG. 6. As in Fig. 5 but now for the high latitude case at 70°N (Tab. 3). Note the different scales with respect to Fig. 5.

definition guarantees that the entire near-surface region affected by radiative heating is included in our analysis.

Fig. 5b shows the evolution of the kinetic energy budget in (24) for the equatorial case. During the initial DWL formation phase until approximately early afternoon, the work performed by the wind, $u^0 \cdot \tau_x^0$, is largely used to accelerate the DWL (see increase in $\frac{\mathrm{d}}{\mathrm{d}t} E_k$) with a significantly smaller contribution used for turbulence shear production $\int P \mathrm{d}z$. In the afternoon, entrainment starts to become increasingly important (Fig. 5a), and additional energy is thus required to accelerate entrained fluid. As a consequence, the DWL kinetic energy increases at a slower rate while shear production becomes the dominant energy sink. After the surface buoyancy forcing collapses in the late afternoon and evening, the entrainment rate further increases as no more work is required to mix down buoyant fluid from the surface (see more detailed discussion below). This point is marked by a sharp transition in the energy budget at approximately 18:00, after which E_k remains constant, and all work performed by the wind is used for turbulence shear production that in turn becomes available for entrainment. Stokes shear production (Fig. 5c) dominates turbulence production during the initial DWL formation phase until approximately noon, while the exchange of mean kinetic energy with the wave field (marked in green in Fig. 5b) is negligible throughout the simulations.

For the high-latitude case shown in Fig. 6, the work performed by the surface stress, $u^0 \cdot \tau_x^0$, starts to be suppressed by the veering of the near-surface velocity out of the wind direction already shortly after the formation of the DWL. This is reflected in a late-morning peak of the wind energy input, and a subsequent monotonic decay down to negative values (energy loss) around 15:00 in the afternoon (Fig. 6b). Therefore, starting from the early afternoon, the pool of DWL kinetic energy built up during the initial DWL formation in the morning becomes an increasingly important energy source ($\frac{\mathrm{d}}{\mathrm{d}t} E_k < 0$) to feed turbulence shear production in the afternoon. Comparison with Fig. 5 shows that due to these effects, the integrated wind work is approximately an order of magnitude smaller compared to the equatorial case, which cannot be explained by the slightly smaller wind stress for the high-latitude case alone (see Tab. 3). Due to the overall strongly reduced energy turnover, the extraction of energy from the wave field due to Coriolis effects (green line in Fig. 6b) becomes significant in the mean kinetic energy budget, and Stokes shear production becomes the dominant term in the TKE budget (blue line in Fig. 6c), despite the fact that P_S is only approximately half as large as in the equatorial case. The net effect of the reduced turbulence production due to rotation is a complete collapse of entrainment almost immediately after the DWL formation in the early morning (green curve in Fig. 6a).

It is worth noting that in simulations without wave effects (not shown), the lacking Stokes shear production P_s is compensated, or even exceeded, by increased Eulerian shear production P in both the equatorial and the high-latitude cases. Reduced near-surface mixing of momentum in these

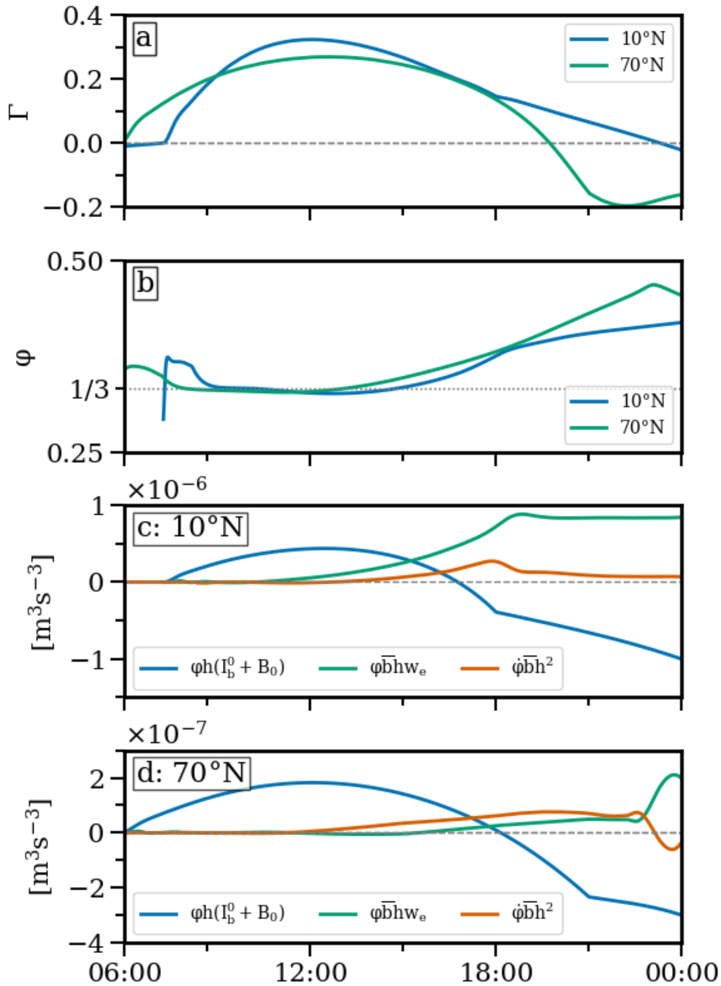

FIG. 7. Evolution of (a) bulk mixing efficiency Γ, (b) shape factor φ computed from (20) based on h from the 5% density threshold (green line in Figs. 5a and 6a), the left hand side terms in (23) at (c) 10°N and (d) 70°N. Note the different axes scales in Panel (c) and (d).

cases (see Fig. 3) leads to larger surface speeds and in turn larger wind work, $\mathbf{u}^0 \cdot \boldsymbol{\tau}^0$, compensating for the lacking energy input from the waves. Although this shift in the primary energy source constitutes a strong modification of the energy budgets, the overall effect on DWL kinetic energy, entrainment, and bulk parameters is surprisingly moderate, as shown in more detail in Section 7.

To investigate to which extent the strong surface buoyancy forcing and the stratification inside the DWL affect the energetics of turbulence, we computed the Ozmidov scale, $L_O = (\varepsilon/N^3)^{1/2}$, as a measure of the vertical size of turbulent overturns. Consistent with the DWL observations of Hughes et al. (2020b) for light and moderate winds (see their Fig. 6), we find typical values of $L_O = 0.1 - 1$ m, suggesting that stratification rather than the proximity to the surface controls the vertical scale of turbulent motions except very close to the surface. Combined with the large values of Ri throughout the DWL (e.g., Fig. 4), we expect mixing inside the DWL to be quite efficient. This is confirmed by the large values of the bulk flux coefficient, $\Gamma = -\int_{z_{\mathrm{ref}}}^{0} G \mathrm{d}z / \int_{z_{\mathrm{ref}}}^{0} \varepsilon \mathrm{d}z$, that we see in all our simulations. While we typically find $\Gamma = 0.15 - 0.2$, close to the popularly used value of $\Gamma = 0.2$, in our simulations without LT, the inclusion of Langmuir effects yields significantly larger values up to $\Gamma = 0.3$ as shown in Fig. 7a. This result is consistent with our LES (not shown).

The different contributions to the potential energy budget in (23) for the tropical and high-latitude cases are compared in Fig. 7c and Fig. 7d, respectively. During the morning and early afternoon, in both cases, by far the largest fraction of the work performed by turbulence against gravity is used to mix near-surface buoyant fluid. The dominance of this term is especially pronounced in the high-latitude case, where entrainment is small after the initial DWL formation phase. Entrainment starts to dominate the energy budget for the tropical case around 15:00, whereas, for the high-latitude case, entrainment never provides a significant contribution except for a short period around sunset. It should be noted that the overall potential energy turnover is a factor 2-3 smaller for the high-latitude case due to the limitation of turbulence production by rotation effects, as explained above.

Beyond the work required for turbulent DWL deepening (entrainment), turbulent mixing may also act to change the vertical DWL buoyancy structure. The energetic implications of this third type of energy conversion that has so far not received much attention can be quantified by considering changes in the shape parameter φ, which is easily computed from (20) after determining the DWL thickness h from the 5% buoyancy threshold discussed above (see green lines in Figs. 5a and 6a). Fig. 7b shows that during the morning and early afternoon, this parameter remains close to $\varphi = 1/3$, consistent with the observed linear stratification seen in Figs. 3, 5a, 6a, but increases to larger values at later times, reflecting the tendency towards a more well-mixed DWL due to the decreasing solar buoyancy forcing. Figs. 7c,d show that the work required for this partial homogenization of the DWL becomes significant in the afternoon for the tropical case, and clearly exceeds the effect of entrainment for the high-latitude case.

7. Parameter-space studies and parameterization

a. Non-dimensional PWP86 model

A frequently used model to describe DWL bulk parameters has been formulated by Price et al. (1986) (from here on PWP86). These authors used a vertically integrated mixed-layer model with a simple parameterization for entrainment (Pollard et al. 1973), forced, as in our study, with a constant wind stress and a surface buoyancy forcing identical to that shown in Fig. 1. Based on a scale analysis of their model equations, PWP86 suggested simple scaling relations for the DWL thickness, h, buoyancy anomaly, $\overline{b}$ (as defined in (20)), and velocity anomaly, $\overline{V} = \sqrt{(\overline{u}^2 + \overline{v}^2)}$ with

$$\overline{u} = \frac{1}{h} \int_{z_{\rm ref}}^{0} \tilde{u} \mathrm{d}z \,, \quad \overline{v} = \frac{1}{h} \int_{z_{\rm ref}}^{0} \tilde{v} \mathrm{d}z \tag{26}$$

and $\tilde{u} = u - u_{\rm ref}$, $\tilde{v} = v - v_{\rm ref}$, all evaluated at the peak buoyancy flux (i.e., at noon). Converted to the notation used in our study, and expressed in non-dimensional form, these scaling relations can be written as:

$$\hat{h} = \frac{h}{L_{MO}} = a_1 \cdot R^{-1/2} F(\hat{f}) \,, \tag{27}$$

$$\hat{\overline{b}} = \frac{\overline{b} u_*}{B_{\rm max}} = a_2 \cdot R^{-1/2} F(\hat{f})^{-1} \,, \tag{28}$$

$$\hat{\overline{V}} = \frac{\overline{V}}{u_*} = a_3 \cdot R^{-1/2} \,, \tag{29}$$

where a_1, a_2, and a_3 denote non-dimensional model constants, and F a non-dimensional model function defined as

$$F(\hat{f}) = \frac{1}{\hat{f}} \left[2 - 2\cos(\hat{f}/2) \right]^{\frac{1}{2}} \,. \tag{30}$$

Note that only two of the non-dimensional parameters identified in Sec. 4b, $R = u_*^2/(B_{\rm max} T_h)$ and $\hat{f}$, appear in the PWP86 model.

b. Parameter space studies

To test the scaling relations by PWP86, we performed a parameter space study in which we varied R from 10^{-4} to 10^{-2} and $\hat{f}$ from 0 to 4.95 (or, equivalently, T_h/T_f from 0 to 0.79). In total, we performed 200 model runs with the same time step and the same number of grid cells as in Sections 5 and 6. However, the depth of the water column was now automatically adjusted to 10 times the DWL thickness at midday to insure that the lower edge of the numerical domain had no significant impact on the results.

We especially focused on the model performance in high-latitude regions ($T_h/T_f \gg 0.1$), which are not well explored at the moment and for which the model assumptions of PWP86 are uncertain. We again assume that all short-wave radiation is absorbed at the surface ($\hat{\eta} = 0$), and that the daily average of the total buoyancy flux is zero ($B_0/B_{\max} = -0.466$, $T_h/T_p = 0.4$). The roughness length is set to $\hat{z}_0 = 0.01$. A sensitivity study, discussed in more detail below, shows that the effect of varying $B_0/B_{\max}$, T_h/T_p, and $\hat{z}$ is small.

In Fig. 8, we show simulation results for the non-dimensional DWL thickness, $\hat{h}$, bulk buoyancy, $\hat{\overline{b}}$, and bulk velocity $\hat{\overline{V}}$ at $t = T_p/2$, i.e. at midday. These quantities are normalized by the PWP86 scaling relations in (27), (28), and (29), respectively, to reveal the variability of the model parameters a_1, a_2, and a_3. Fig. 8 shows that the performance of the PWP86 scaling is generally excellent, except for a weakly forced regime with $R \lessapprox 7 \cdot 10^{-4}$ (blue dashed line in Fig. 8), where a strong variability in the PWP86 model parameters suggests that their scaling fails.

A more detailed analysis showed that turbulent and molecular diffusivities become comparable in this regime, and that Ri at the DWL base becomes much larger than the critical value for shear instability, indicating a collapse of turbulent entrainment. It is worth noting that Hughes et al. (2020a) studied this regime in more detail, based on high-resolution observations and a 1D model with a simpler turbulence closure without LT but similar radiative and atmospheric forcing parameters. From their simulations, these authors identified a critical wind speed of $U_{10} = 2$ m s^{-1} below which turbulent mixing collapses. This is equivalent to $R = 6.6 \cdot 10^{-4}$, and therefore consistent with the more generally applicable non-dimensional threshold suggested by our simulations with a more advanced turbulence model that also included Langmuir effects. Overall, this indicates that due to strong molecular effects, turbulence in this parameter range and can no

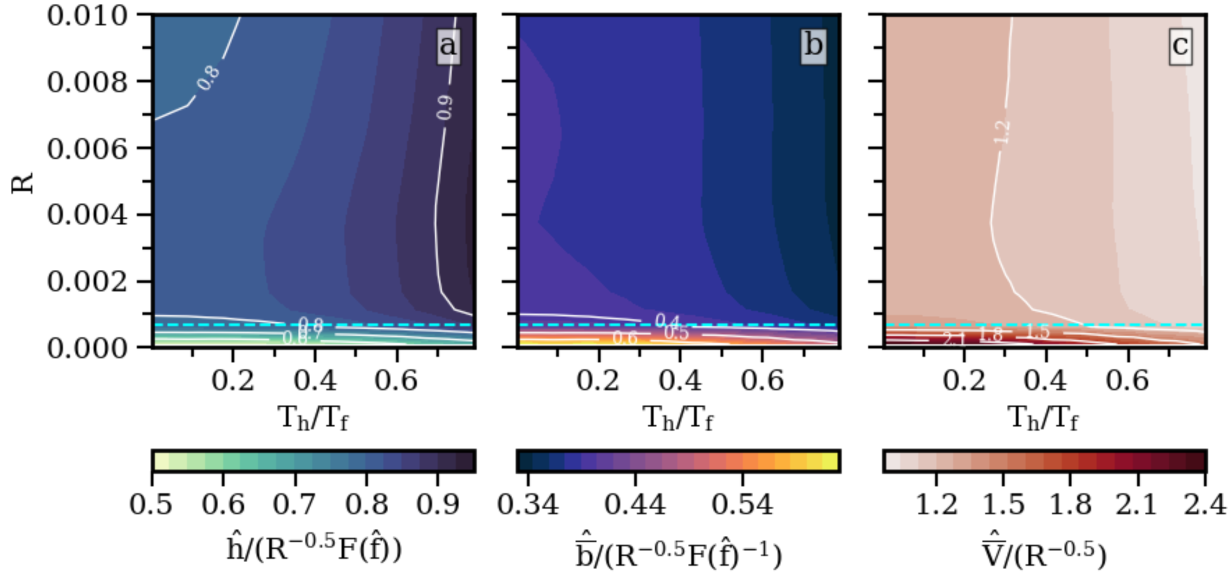

FIG. 8. DWL properties as functions of $R = u_*^2/(B_{\max} T_h)$ and $T_h/T_f = \hat{f}/(2\pi)$. Shown are midday values of (a) DWL thickness, (b) DWL bulk buoyancy, and (c) DWL bulk velocity, normalized by the PWP86 scalings in (27), (28), and (29). This implies that the results shown in (a)-(c) correspond to PWP86 model constants a_i. The blue line shows the critical value of R below which DWL turbulence starts to collapse.

longer reliably be represented by any of the high-Reynolds number turbulence models used in our study. We therefore don't investigate this regime any further here.

We determined the model constants a_1, a_2, and a_3 by calculating the mean of the PWP86-scaled model results shown in Fig. 8 , excluding regions with $R < 7 \cdot 10^{-4}$. Tab. 4 shows that deviations from these constant values rarely exceed 10% (with largest deviations observed at large T_h/T_f), confirming the validity of the PWP86 scaling across the entire parameter range. This is a surprising result, as some of the model assumptions in PWP86 are not valid any more at high latitudes. It is worth noting from Tab. 4 that our revised constants suggest a 32% larger DWL thickness, a 39% smaller DWL buoyancy anomaly, and a 12% faster surface jet at midday compared to the original model constants of PWP86, which is clearly significant even for rough estimates of the DWL bulk properties. Only part of these differences can be attributed to the effects of LT not accounted for in PWP86. Tab. 4 shows that simulations without LT (not discussed in detail here) result in DWLs that are approximately 10% shallower and have a correspondingly larger buoyancy contrast.

TABLE 4. Model constants a_1, a_2 and a_3 of the PWP86 model appearing in (27)–(29). The original constants of PWP86 were converted to our notation according to: $a_1 = 0.45 \cdot 2^{1/2} = 0.63$, $a_2 = 1.5 \cdot 2^{-3/2} = 0.53$ and $a_3 = 1.5 \cdot 2^{-1/2} = 1.06$. The factor $1/2$ arises from the relation $T_h = 2P_Q$, where P_Q is the heating period in the notation of PWP86. The ranges given in the table correspond to the *maximum* deviations across the entire parameter range. Standard deviations (not shown) are considerably smaller. $t_{\max}$ is the time of maximum buoyancy anomaly.

	$t = T_p/2$			$t = t_{\max}$	
	PWP86	with LT	without LT	with LT	without LT
a_1	0.63	0.84 ± 0.07	0.75 ± 0.1	1.08 ± 0.03	1.01 ± 0.05
a_2	0.53	0.38 ± 0.03	0.42 ± 0.05	0.56 ± 0.05	0.59 ± 0.05
a_3	1.06	1.15 ± 0.15	1.30 ± 0.2	1.3 ± 0.5	1.3 ± 0.5

The PWP86 scaling relations were originally proposed to predict DWL properties at the solar radiation peak ($t = T_p/2$). More relevant for the surface-layer energetics, atmosphere-ocean coupling, and ecosystem applications, are, however, often the DWL properties at peak of the DWL buoyancy or temperature anomaly in the afternoon. This point during the diurnal cycle cannot be determined from the PWP86 scaling. We therefore identified the (non-dimensional) time $t_{\max}/T_p$ of the maximum buoyancy anomaly numerically from our simulations. Fig. 9a shows that the DWL buoyancy anomaly peaks between approximately 15:00 and 16:00 (assuming $T_p = 24$ h) with a shift towards later times for larger T_h/T_f. We attribute this shift to the suppression of entrainment of colder bottom waters due to stronger rotation effects at higher latitudes and/or a larger total buoyancy flux for larger T_h. In view of the comparatively weak dependency on R visible in Fig. 9a, we averaged over the entire range of R to obtain the simple fit shown in Fig. 9b:

$$t_{\max}/T_p = 0.09 \left(\frac{T_h}{T_f} \right)^{1.6} + 0.63 \,, \tag{31}$$

which may be useful for a quick computation of $t_{\max}$ (recall that $t/T_p = 0$ corresponds to the start of all simulations at midnight).

Scaling our simulations at $t = t_{\max}$ with the expressions of PWP86 (see Fig. 10) suggests that the PWP86 scaling provides an excellent representation of the DWL bulk properties also during the buoyancy peak in the afternoon, provided the model coefficients a_1, a_2, and a_3 are adjusted

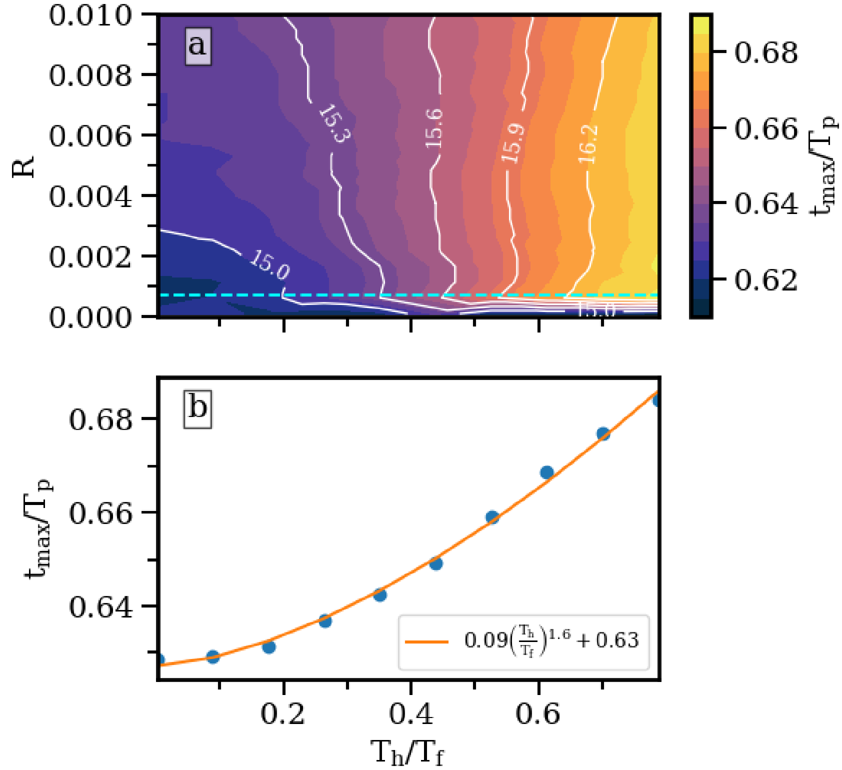

FIG. 9. Time $t_{\max}/T_p$ of the maximum buoyancy anomaly for (a) varying R and T_h/T_f (the contour line labels show the time in hours of the day) and (b) the mean $t_{\max}/T_p$ for $R > 7 \cdot 10^{-4}$ as a function of T_h/T_f.

from their PWP86 values. The values in Tab. 4 show that the DWL thickness and the buoyancy anomaly have increased by 29% and 47%, respectively, compared to midday, illustrating a strong modification of the DWL during the early afternoon. The small variability of the model coefficients in Tab. 4 supports the quality of the fit, except for the near-surface jet, which shows a strong dependency on T_h/T_f especially for large values of this parameter (see Fig. 10c). We attribute this to the effect of the pronounced inertial oscillations at high latitudes that are not well represented by the scaling of PWP86.

Finally, as shown in Fig. 11, we find that the non-dimensional parameters T_h/T_p, $B_0/B_{\max}$, $\hat{z}_0$, and $\hat{k}_p$, ignored so far, have a negligible impact on the non-dimensional DWL thickness $\hat{h}$ (and also on the other DWL bulk properties not shown here for brevity). We note, however, that the parameters T_h/T_p and $B_0/B_{\max}$ may have a larger impact for longer simulation periods of several days, where they may affect the nighttime DWL reset and thus the quasi-periodic evolution of the surface layer

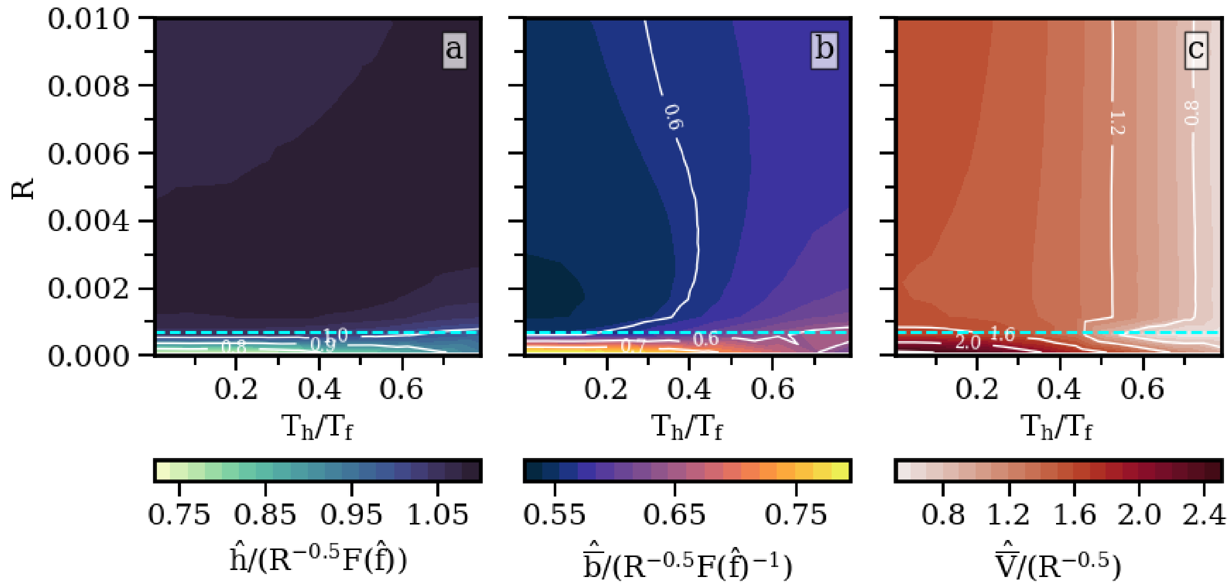

FIG. 10. As in Fig. 8, but now for $t = t_{\max}$, i.e. the time of the maximum buoyancy anomaly in the afternoon.

structure. Similarly, the peak wavenumber $\hat{k}_p$ may become relevant for non-equilibrium wave fields, especially for conditions when long-wave swell induces a larger penetration depth of the Stokes shear.

c. Effect of short-wave absorption

To study the effect of the remaining non-dimensional parameter, the non-dimensional short-wave penetration depth $\hat{\eta}$ introduced via (5), we carried out two parameter space studies similar to that shown in Fig. 8. In these cases, however, we varied R and $\hat{\eta}$ over the ranges $R = 10^{-4} - 10^{-2}$ and $\hat{\eta} = 0 - 5$, at two different latitudes. We chose $T_h/T_f = 0.14$ and 0.94, corresponding to our standard tropical and high-latitude cases from Section 6, while keeping the other non-dimensional parameters constant at $T_h/T_p = 0.4$, $B_0/B_{\max} = -0.466$ and $\hat{z}_0 = 0.01$. Each parameter space again consists of 200 model runs. Consistent with the destabilizing (with respect to $\hat{\eta} = 0$) effect of penetrating short-wave radiation, we observe an increase of $\hat{h}$ for increasing $\hat{\eta}$, especially for large R, while $\hat{\overline{b}}$ and $\hat{\overline{V}}$ decrease (the according plots can be found in the supplementary material).

Following PWP86, it appears physically sensible to express the destabilizing effect of increasing η by the ratio η/h rather than directly by $\hat{\eta} = \eta/L_{\text{MO}}$. We therefore suggest that the observed increase of the DWL thickness $\hat{h}$ due to an increase in η can be parameterized by multiplying the

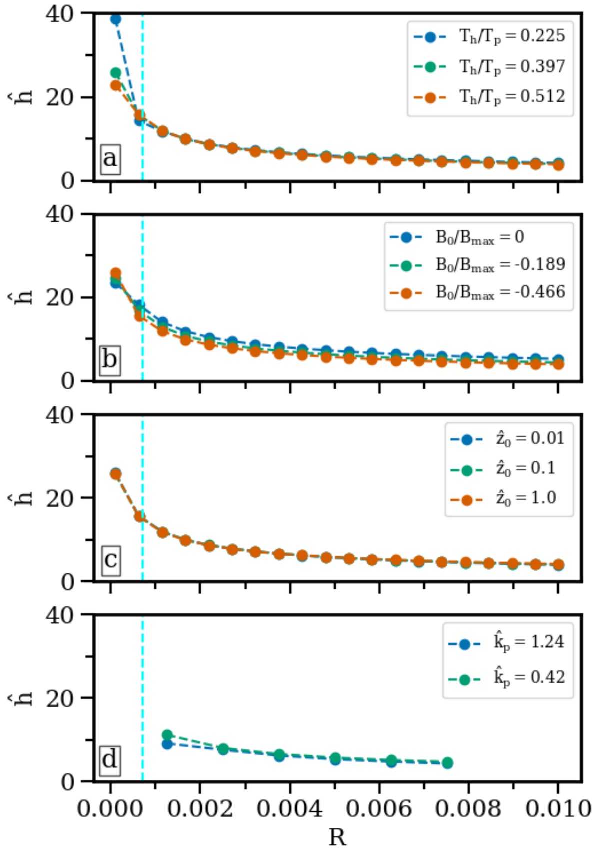

FIG. 11. Non-dimensional thickness $\hat{h}$ for constant $T_h/T_f = 0.14$ as a function of $R = u_*^2/(B_{\max}T_h)$ for different values of (a) the time scale ratio T_h/T_p, (b) the flux ratio $B_0/B_{\max}$, (c) the non-dimensional surface roughness $\hat{z}_0$, and (d) the non-dimensional peak wave number $\hat{k}_p$. Parameters not varied are kept fixed at $T_h/T_p = 0.397$, $B_0/B_{\max} = 0.466$ and $\hat{z}_0 = 0.01$, respectively. The blue line shows the critical threshold for the collapse of DWL turbulence, $R = 7 \cdot 10^{-4}$.

corresponding PWP86 expression in (27) with a function G that depends on η/h, or, equivalently, on $\hat{h}/\hat{\eta}$. In view of the exponential light attenuation, we follow the suggestion of PWP86,

$$G(\hat{h}/\hat{\eta}) = \left(1 - A_\eta e^{-\hat{h}/\hat{\eta}}\right)^{-\frac{3}{2}} \tag{32}$$

with the difference, however, that $A_\eta = 6.9$ was obtained from fitting (the original pre-factor of PWP86 did not yield acceptable results).

TABLE 5. Model constants a_1, a_2 and a_3 at $t = T_p/2$ of the modified PWP86 scaling relations in (33)–(35), evaluated for two different latitudes.

	10°N	70°N
a_1	0.83 ± 0.14	0.83 ± 0.3
a_2	0.38 ± 0.05	0.38 ± 0.2
a_3	1.20 ± 0.3	1.20 ± 0.4

The modified PWP86 scaling that includes the effects of absorption is then given as

$$\hat{h} = a_1 \cdot R^{-1/2} F(\hat{f}) G(\hat{h}/\hat{\eta}) \, , \tag{33}$$

$$\hat{\overline{b}} = a_2 \cdot R^{-1/2} F(\hat{f})^{-1} G(\hat{h}/\hat{\eta})^{-1} \, , \tag{34}$$

$$\hat{\overline{V}} = a_3 \cdot R^{-1/2} G(\hat{h}/\hat{\eta})^{-1/3} \, , \tag{35}$$

where the model constants a_i remain unchanged for consistency with (27)–(29). As $\hat{h}$ is unknown, (33) forms an implicit non-linear equation that needs to be solved numerically. Alternatively, $\hat{h}$ appearing on the right hand side could be approximated by the original expression in (27), Tab. 5 shows that maximum deviations from the standard model constants a_i, and thus the model uncertainties, based on (33)–(35), however, using a DWL thickness that we directly diagnosed from our model results. The variability of the parameters in Tab. 5 suggest that the model uncertainties are still acceptable for the tropical cases but strongly increase for the high-latitude simulations. Furthermore, when $\hat{h}$ is unknown and instead the scaling in (27) is used in (13), the maximum deviations become even more severe.

We conclude that a proper scaling for the absorption of short wave radiation and its effects on DWLs needs future work that is, for now, outside of the scope of this paper.

8. Discussion and conclusions

Based on state-of-the-art second-moment turbulence modeling, and supported by turbulence-resolving LES, we have shown that LT strongly impacts on the DWL energetics, mainly by reducing the work performed by the surface stress and partly compensating this effect by Stokes shear production. The overall impact of this shift in the primary energy source for turbulence on the DWL bulk parameters, however, turned out to be surprisingly moderate. The simulations in Section

7 showed that LT increases the DWL thickness by only 10%, approximately, across a wide parameter range. We attribute this largely to the equilibrium wave model used in our study (Appendix A2), predicting only small wave heights and wave lengths for the weak to moderate winds at which DWLs are observed. Although equilibrium wave fields are typical in many situations, it is worth noting that previous LES studies with monochromatic non-equilibrium waves, focusing on swell effects (Kukulka et al. 2013), have shown a stronger impact of LT on DWL properties. It would therefore be worthwhile to explore the performance of the second-moment models used in our study also in this parameter range, and to understand how the observed effects can be parameterized in terms of the non-dimensional wave parameters La and $\hat{k}_p$ identified in Section 4.

Dimensional analysis and the parameter space studies in Section 7 showed that the most relevant non-dimensional parameters among those compiled in Tab. 2 are: the stability parameter $R = u_*^2/(B_{\max} T_h)$, the time scale ratio T_h/T_f, and, for penetrating short-wave radiation, the non-dimensional absorption scale $\hat{\eta} = \eta/L_{MO}$. Parameterizations that do not independently account for these parameters are unlikely to be generally applicable. One example is the recent DWL parameterization of Wang et al. (2023), who, for constant La, suggested a dependency on the single non-dimensional parameter $\hat{B}_0 \propto (\hat{f} R)^{-1}$, which is unlikely to hold outside the range of latitudes and optical water properties for which their model was calibrated.

As shown in Section 7, however, the three key parameters identified above do appear independently in the frequently used DWL scaling relations of PWP86. We showed that their model reliably predicts the most important DWL bulk parameters across a wide parameter range, provided that their model constants a_1, a_2, and a_3 are significantly revised as summarized in Tabs. 4 and 5. One caveat, however, applies to the low-energy regime with $R = u_*^2/(B_{\max} T_h) < 7 \cdot 10^{-4}$, where molecular effects become important, and the high-Reynolds number models and parameterizations used in this study are no longer applicable. Direct Numerical Simulations appear to be the only viable approach to explore this parameter range, which is relevant especially for very thin DWLs with weak wind forcing and strong buoyancy forcing.

The excellent performance of the simple PWP86 scaling relations was a somewhat unexpected result as our parameter space also included high-latitude DWLs for which some of the PWP86 modeling assumptions formally break down. In view of increasing ice-free areas at high latitudes and strong DWL temperature anomalies already observed at high latitudes (Jia et al. 2023; Eastwood et al. 2011), it is likely that the physics of these DWLs (e.g., Sutherland et al. 2016) will receive increased attention in the future. Finally, we would like to note that DWL bulk parameters predicted by the model of KC04 were nearly indistinguishable from those of HC15, despite significant differences found in the DWL energetics. From a practical point of view, and for the special case of equilibrium wave fields considered here, it is therefore possible to work with the less complex model of KC04, which, e.g., avoids the introduction of a second (Stokes) diffusivity in (12).

Acknowledgments. This paper is a contribution to the project L4 (Energy-Consistent Ocean-Atmosphere Coupling) of the Collaborative Research Centre TRR 181 ”Energy Transfers in Atmosphere and Ocean”, funded by the German Research Foundation (DFG) under grant 274762653 to L. Umlauf. H. T. Pham and S. Sarkar are pleased to acknowledge funding by NSF grant OCE-1851390.

Data availability statement. Simulations in this manuscript were carried out with a modified version of the General Ocean Turbulence Model (GOTM). The used source code is archived at `https://doi.org/10.5281/zenodo.8103884` (Klingbeil and Umlauf 2023). The LES data as well as the scripts that run GOTM and plot the figures shown in this article are archived at `https://doi.org/10.5281/zenodo.8075082` (Schmitt 2023).

APPENDIX

A1. Second-Moment Turbulence Model

The turbulent kinetic energy, k, required to evaluate the expressions for the turbulent diffusivities in (14) is computed from a well-known transport equation of the form:

$$\frac{\partial k}{\partial t} = D_k + P + P_s + G - \varepsilon \, , \tag{A1}$$

generalized here to also account for the effects of Langmuir turbulence (LT). Here, D_k denotes the divergence of the total vertical flux of TKE, G the turbulent buoyancy flux defined in (13), and ε the turbulence dissipation rate. P and P_s are the Eulerian and Stokes shear production terms defined as (Harcourt 2013, 2015):

$$P = -\langle u'w' \rangle \frac{\partial u}{\partial z} - \langle v'w' \rangle \frac{\partial v}{\partial z} = \nu_t S^2 + \nu_t^S S_c^2 \, , \tag{A2}$$

$$P_s = -\langle u'w' \rangle \frac{\partial u_s}{\partial z} - \langle v'w' \rangle \frac{\partial v_s}{\partial z} = \nu_t S_c^2 + \nu_t^S S_s^2 \, , \tag{A3}$$

using the definitions in (15) for the vertical shear terms. For second-moment models that ignore the direct effects of Stokes shear on the stability functions (e.g., KC04), we have $\nu_t^S = 0$, and the above expressions simplify accordingly.

Following work by KC04 and H15 on the parameterization of LT effects on the turbulent length scale, l, we compute this quantity from a modified Mellor-Yamada-type transport equation for the variable kl. Theses authors suggested to include an extra Stokes production term, analogous to the TKE budget in (A1), in the original kl-equation of Mellor and Yamada (1982), leading to an expression of the form:

$$\frac{\partial kl}{\partial t} = D_l + l(c_{l1}P + c_{l4}P_s + c_{l3}G - c_{l2}F\varepsilon) \ , \tag{A4}$$

where the wall function $F = 1 + c_F\left(\frac{l}{\kappa L_z}\right)^2$ (here, κ is the von Kármán constant and L_z the distance from the surface) is required to reproduce the logarithmic wall layer distribution close to the surface. D_l summarizes the vertical transport terms, and c_{l1}–c_{l4} and c_F denote non-dimensional model constants (or functions) discussed in more detail below. Note that the kl-equation in (A4) is expressed here in the notation of the "generic length scale" (GLS) framework (Umlauf and Burchard 2003) for easier comparison with other model equations. The conversion relations between our notation and that originally used by KC04 and H15 are summarized in Tab. A1. The stability functions appearing in (14) are related to their equivalents in Mellor-Yamada notation (see H15) as $c_\mu = 2^{1/2}S_M$, $c_\mu^S = 2^{1/2}S_M^S$, and $c_\mu^b = 2^{1/2}S_H$.

As an alternative to the transport equation for kl in (A4), we also computed some of the solutions based on the k-ω model by Umlauf et al. (2003), solving (A1) combined with an equation of the form

$$\frac{\partial \omega}{\partial t} = D_\omega + \frac{\omega}{k}\left(c_{\omega 1}P + c_{\omega 4}P_s + c_{\omega 3}G - c_{\omega 2}\varepsilon\right) \ , \tag{A5}$$

where ω denotes an inverse turbulence time scale defined as

$$\omega = (c_\mu^0)^{-4}\varepsilon k^{-1} \ . \tag{A6}$$

Similar to (A4), the transport equation for ω in (A5) includes a Stokes production term recently suggested by Yu et al. (2022) to account for LT effects. D_ω denotes again the turbulent transport terms, and $c_{\omega 1}$–$c_{\omega 4}$ are non-dimensional model constants (see Tab. A1).

The transport terms D_k, D_l, and D_ω appearing in (A1), (A4), and (A5), respectively, are modeled by down-gradient expressions:

$$D_k = \frac{\partial}{\partial z}\left(\nu_t^k \frac{\partial k}{\partial z}\right), \quad D_l = \frac{\partial}{\partial z}\left(\nu_t^l \frac{\partial kl}{\partial z}\right), \quad D_\omega = \frac{\partial}{\partial z}\left(\nu_t^\omega \frac{\partial \omega}{\partial z}\right), \tag{A7}$$

where $\nu_t^k = c_\mu^k k^{\frac{1}{2}} l$, $\nu_t^l = c_\mu^l k^{\frac{1}{2}} l$ and $\nu_t^\omega = c_\mu^\omega k^{\frac{1}{2}} l$, are turbulent diffusivities, and c_μ^k, c_μ^l, and c_μ^ω the corresponding stability functions.

The model parameters c_{l1} and c_{l2}, and similarly $c_{\omega 1}$ and $c_{\omega 2}$ for the k-ω model (all compiled in Tab. A1) are well constrained by classical data for unstratified shear layers and decaying turbulence (e.g., Umlauf and Burchard 2003). The parameters c_{l3} and $c_{\omega 3}$ are essential for this study as they determine the entrainment rate in stratified turbulent boundary layers. Their values follow from a condition on the so-scalled steady-state Richardson number, Ri_{st}, corresponding to the value of the Richardson number Ri in the entrainment layer at the base of the turbulent surface layer (Umlauf and Burchard 2005). Here, we use $Ri_{st} = 0.23$ (the maximum value permitted by the stability functions of KC04 and H15), yielding the c_{l3} and $c_{\omega 3}$ shown in Tab. A1. Note that $c_{l3} = 2.4$ corresponds to $E_3 = 4.8$ in Mellor-Yamada notation, which is close to the value $E_3 = 5.0$ used by H15. We also follow the suggestion by H15 to limit the vertical length scale by the Ozmidov scale, $L_O = (\varepsilon N^{-3})^{1/2}$, as originally suggested by Galperin et al. (1988), noting, however, that this only marginally changes the results. For the wall model constant c_F (or E_4 in the notation of KC04 and H15), we follow Harcourt (2013), who suggested $E_4 = 1.33(1+0.5\mathrm{La}^{-2})^{1/3} = 2.9$ with a Langmuir number of $\mathrm{La} = 0.3$ to account for the modified near-surface slope of the turbulent length scale due to LT (La is defined in Appendix A2). For our simulations without LT effects, this expression reduces to the traditional value $E_4 = 1.33$.

The most important model parameters in (A4) and (A5) in the context of LT are those multiplying the Stokes shear production terms, respectively. For the kl-equation, we adopt H15's value $E_6 = 6$, corresponding to $c_{l4} = 3$ in GLS notation (Tab. A1). Note that this value is close to the revised $E_6 = 7.2$ obtained from comparison to field measurements (see Kantha et al. 2010) of KC04. For the k-ω model, we follow Yu et al. (2022) and choose $c_{\omega 4} = 0.15$.

As in the original model of Kantha and Clayson (1994) without LT effects, also in KC04, the stability functions for the transport terms in (A7) reduce to constants. KC04 suggested $S_l/S_q = 3.7$

TABLE A1. Non-dimensional model constants as in (A1), (A4) and (A5).

GLS notation		KC04 and H15 notation		ω	
c_{l1}	0.9	$E_1 = 2c_1$	1.8	$c_{\omega 1}$	0.55
c_{l2}	0.5	$E_2 = 2c_2$	1.0	$c_{\omega 2}$	0.83
c_{l3}	2.4	$E_3 = 2c_3$	4.8	$c_{\omega 3^-}$	-0.52
c_{l4}	3.0	$E_6 = 2c_4$	6.0	$c_{\omega 4}$	0.15
c_F	1.45	$E_4 = 2c_F$	2.9	-	-
c_μ^k	0.28	$S_q = 2^{-1/2}c_\mu^k$	0.2*	†	
c_μ^l	0.28	$S_l = 2^{-1/2}c_\mu^l$	0.2*	†	
c_μ^0	0.55	$B_1 = 2^{3/2}(c_\mu^0)^{-3}$	16.6	c_μ^0	0.55

*: Only for KC04. For H15, these change according to (A8)

†: $c_\mu^{k,\omega} = c_\mu/\sigma_{k,\omega}$ with $\sigma_{k,\omega} = 2.0$

but, similar to Harcourt (2013), we find that $S_l = S_q = 0.2$ is more in line with the LES results. For H15, the stability functions are defined as

$$S_q = S_l = [0.2^2 + (0.41 S_H)^2]^{1/2}, \tag{A8}$$

to account for the enhanced transport due to LT (here, S_H is the stability function for the turbulent diffusivity of heat, c_μ^b in our notation). For the k-ω model, the stability functions c_μ^k and c_μ^ω are chosen proportional to c_μ (see Umlauf et al. 2003) with constant proportionality factors expressed in terms of the turbulent Schmidt numbers σ_k and σ_ω (see Tab. A1).

Finally, we use the following boundary conditions for (A1) and (A4):

$$k = \frac{u^{*2}}{(c_\mu^0)^2} \quad \text{at} \quad z = 0 \quad , \qquad \frac{\partial k}{\partial z} = 0 \quad \text{at} \quad z = -\infty \tag{A9}$$

$$l = \kappa z_0 \quad \text{at} \quad z = 0 \quad , \qquad \frac{\partial kl}{\partial z} = 0 \quad \text{at} \quad z = -\infty\,, \tag{A10}$$

where z_0 is the surface roughness length. For the upper boundary, these boundary conditions follow from the classical law-of-the-wall relations (see Umlauf and Burchard 2005).

It is important to note that for the case of vanishing surface-wave forcing $u_s = v_s = 0$ the models of both KC04 and H15 reduce to the original model of Kantha and Clayson (1994), except for some minor differences in some of the model constants.

A2. Empirical Wave Model

Surface wave parameters in our study are computed from the ”Theory Wave” approach of Li et al. (2017), which summarized the state-of-the-art surface-wave modeling components used in their method. In this model, the surface Stokes drift velocity, u_s^0, and the Stokes transport, V_s, are estimated from expressions of the form

$$u_s^0 = c_s U_{10} \, , \quad V_s = C_s \frac{U_{10}^3}{g} \, , \tag{A11}$$

where U_{10} denotes the 10-m wind speed, and $c_s = 0.016$ and $C_s = 2.56 \cdot 10^{-3}$ are non-dimensional model constants (note that the wind and thus the Stokes velocity always point into the x-direction in our simulations).

The spectral peak wave number, k_p, and the peak wave number including wave spreading effects, k_p^*, in the model of Li et al. (2017) are

$$k_p \approx 0.176 \frac{u_s^0}{V_s} \, , \quad k_p^* = 2.56 k_p \, . \tag{A12}$$

Based on a simple model spectrum, Li et al. (2017) showed that the vertically averaged Stokes velocity,

$$\overline{u}_s = \frac{1}{z} \int_z^0 u_s \mathrm{d}z^* \, , \tag{A13}$$

can be described in the following form:

$$\begin{aligned} \overline{u}_s \approx u_s^0 \Bigg\{ & 0.715 + \left(\frac{0.151}{k_p z} - 0.840 \right) [1 - T_1(k_p, z)] - \left(0.840 + \frac{0.0591}{k_p z} \right) T_2(k_p, z) \\ & + \left(\frac{0.0632}{k_p^* z} + 0.125 \right) [1 - T_1(k_p^*, z)] + \left(0.125 + \frac{0.0946}{k_p^* z} \right) T_2(k_p^*, z) \Bigg\} \end{aligned} \tag{A14}$$

where

$$T_1(k_p, z) = 2 \mathrm{e}^{k_p z} \tag{A15}$$

$$T_2(k_p, z) = \sqrt{2\pi k_p |z|} \operatorname{erfc}\left(\sqrt{2 k_p |z|} \right) . \tag{A16}$$

From (A13), it is clear that the local Stokes velocity follows from

$$u_s = -\frac{\partial \overline{u}_s z}{\partial z} , \tag{A17}$$

which we use to compute the Stokes shear (15) .

References

Bellenger, H., and J.-P. Duvel, 2009: An Analysis of Tropical Ocean Diurnal Warm Layers. *J. Clim.*, **22 (13)**, 3629–3646, https://doi.org/10.1175/2008JCLI2598.1.

Brilouet, P.-E., J.-L. Redelsperger, M.-N. Bouin, F. Couvreux, and C. Lebeaupin Brossier, 2021: A case-study of the coupled ocean–atmosphere response to an oceanic diurnal warm layer. *Q. J. R. Meteorol. Soc.*, **147 (736)**, 2008–2032, https://doi.org/10.1002/qj.4007.

Ducros, F., P. Comte, and M. Lesieur, 1996: Large-eddy simulation of transition to turbulence in a boundary layer developing spatially over a flat plate. *Journal of Fluid Mechanics*, **326**, 1–36, https://doi.org/10.1017/S0022112096008221.

Eastwood, S., P. Le Borgne, S. Péré, and D. Poulter, 2011: Diurnal variability in sea surface temperature in the Arctic. *Remote Sensing of Environment*, **115 (10)**, 2594–2602, https://doi.org/10.1016/j.rse.2011.05.015.

Galperin, B., L. H. Kantha, S. Hassid, and A. Rosati, 1988: A Quasi-equilibrium Turbulent Energy Model for Geophysical Flows. *J. Atmospheric Sci.*, **45 (1)**, 55–62, https://doi.org/10.1175/1520-0469(1988)045⟨0055:AQETEM⟩2.0.CO;2.

Harcourt, R. R., 2013: A Second-Moment Closure Model of Langmuir Turbulence. *J. Phys. Oceanogr.*, **43 (4)**, 673–697, https://doi.org/10.1175/JPO-D-12-0105.1.

Harcourt, R. R., 2015: An Improved Second-Moment Closure Model of Langmuir Turbulence. *J. Phys. Oceanogr.*, **45 (1)**, 84–103, https://doi.org/10.1175/JPO-D-14-0046.1.

Hughes, K. G., J. N. Moum, and E. L. Shroyer, 2020a: Evolution of the Velocity Structure in the Diurnal Warm Layer. *J. Phys. Oceanogr.*, **50 (3)**, 615–631, https://doi.org/10.1175/JPO-D-19-0207.1.

Hughes, K. G., J. N. Moum, and E. L. Shroyer, 2020b: Heat Transport through Diurnal Warm Layers. *J. Phys. Oceanogr.*, **50 (10)**, 2885–2905, https://doi.org/10.1175/JPO-D-20-0079.1.

Jia, C., P. J. Minnett, and B. Luo, 2023: Significant Diurnal Warming Events Observed by Saildrone at High Latitudes. *Journal of Geophysical Research: Oceans*, **128 (1)**, e2022JC019 368, https://doi.org/10.1029/2022JC019368.

Kantha, L., H. U. Lass, and H. Prandke, 2010: A note on Stokes production of turbulence kinetic energy in the oceanic mixed layer: Observations in the Baltic Sea. *Ocean Dynamics*, **60 (1)**, 171–180, https://doi.org/10.1007/s10236-009-0257-7.

Kantha, L. H., and A. C. Clayson, 2004: On the effect of surface gravity waves on mixing in the oceanic mixed layer. *Ocean Modelling*, **6 (2)**, 101–124, https://doi.org/10.1016/S1463-5003(02)00062-8.

Kantha, L. H., and C. A. Clayson, 1994: An improved mixed layer model for geophysical applications. *J. Geophys. Res. Oceans*, **99 (C12)**, 25 235–25 266, https://doi.org/10.1029/94JC02257.

Kawai, Y., and A. Wada, 2007: Diurnal sea surface temperature variation and its impact on the atmosphere and ocean: A review. *J Oceanogr*, **63 (5)**, 721–744, https://doi.org/10.1007/s10872-007-0063-0.

Klingbeil, K., and L. Umlauf, 2023: GOTM source code with langmuir turbulence closure. Zenodo, URL https://doi.org/10.5281/zenodo.8103884.

Kukulka, T., A. J. Plueddemann, and P. P. Sullivan, 2013: Inhibited upper ocean restratification in nonequilibrium swell conditions. *Geophys. Res. Lett.*, **40 (14)**, 3672–3676, https://doi.org/10.1002/grl.50708.

Large, W. G., and J. M. Caron, 2015: Diurnal cycling of sea surface temperature, salinity, and current in the CESM coupled climate model. *J. Geophys. Res. Oceans*, **120 (5)**, 3711–3729, https://doi.org/10.1002/2014JC010691.

Li, Q., B. Fox-Kemper, Ø. Breivik, and A. Webb, 2017: Statistical models of global Langmuir mixing. *Ocean Modelling*, **113**, 95–114, https://doi.org/10.1016/j.ocemod.2017.03.016.

Matthews, A. J., D. B. Baranowski, K. J. Heywood, P. J. Flatau, and S. Schmidtko, 2014: The Surface Diurnal Warm Layer in the Indian Ocean during CINDY/DYNAMO. *J. Clim.*, **27 (24)**, 9101–9122, https://doi.org/10.1175/JCLI-D-14-00222.1.

Mellor, G. L., and T. Yamada, 1982: Development of a turbulence closure model for geophysical fluid problems. *Rev. Geophys.*, **20 (4)**, 851–875, https://doi.org/10.1029/RG020i004p00851.

Moulin, A. J., J. N. Moum, and E. L. Shroyer, 2018: Evolution of Turbulence in the Diurnal Warm Layer. *J. Phys. Oceanogr.*, **48 (2)**, 383–396, https://doi.org/10.1175/JPO-D-17-0170.1.

Pham, H. T., S. Sarkar, L. Johnson, B. Fox-Kemper, P. P. Sullivan, and Q. Li, 2023: Multi-Scale Temporal Variability of Turbulent Mixing During a Monsoon Intra-Seasonal Oscillation in the Bay of Bengal: An LES Study. *Journal of Geophysical Research: Oceans*, **128 (1)**, e2022JC018 959, https://doi.org/10.1029/2022JC018959.

Pollard, R. T., P. B. Rhines, and R. O. Thompson, 1973: The deepening of the wind-mixed layer. *Geophys. Astrophys. Fluid Dyn.*, **4 (1)**, 381–404.

Price, J. F., R. A. Weller, and R. Pinkel, 1986: Diurnal cycling: Observations and models of the upper ocean response to diurnal heating, cooling, and wind mixing. *J. Geophys. Res. Oceans*, **91 (C7)**, 8411–8427, https://doi.org/10.1029/JC091iC07p08411.

Sarkar, S., and H. T. Pham, 2019: Turbulence and Thermal Structure in the Upper Ocean: Turbulence-Resolving Simulations. *Flow Turbulence Combust*, **103 (4)**, 985–1009, https://doi.org/10.1007/s10494-019-00065-5.

Schmitt, M., 2023: Scripts for ’Diurnal Warm Layers in the Ocean: Energetics, Non-dimensional Scaling, and Parameterization’. Zenodo, URL https://doi.org/10.5281/zenodo.8075082.

Sutherland, G., L. Marié, G. Reverdin, K. H. Christensen, G. Broström, and B. Ward, 2016: Enhanced Turbulence Associated with the Diurnal Jet in the Ocean Surface Boundary Layer. *J. Phys. Oceanogr.*, **46 (10)**, 3051–3067, https://doi.org/10.1175/JPO-D-15-0172.1.

Suzuki, N., and B. Fox-Kemper, 2016: Understanding Stokes forces in the wave-averaged equations. *Journal of Geophysical Research: Oceans*, **121 (5)**, 3579–3596, https://doi.org/10.1002/2015JC011566.

Umlauf, L., and H. Burchard, 2003: A generic length-scale equation for geophysical turbulence models. *J. Mar. Res.*, **61 (2)**, 235–265, https://doi.org/10.1357/002224003322005087.

Umlauf, L., and H. Burchard, 2005: Second-order turbulence closure models for geophysical boundary layers. A review of recent work. *Continental Shelf Research*, **25 (7)**, 795–827, https://doi.org/10.1016/j.csr.2004.08.004.

Umlauf, L., H. Burchard, and K. Bolding, 2005: GOTM - Scientic Documentation : Version 3.2. **63**, 279, https://doi.org/10.12754/MSR-2005-0063.

Umlauf, L., H. Burchard, and K. Hutter, 2003: Extending the k–ω turbulence model towards oceanic applications. *Ocean Modelling*, **5 (3)**, 195–218, https://doi.org/10.1016/S1463-5003(02)00039-2.

Wang, X., T. Kukulka, J. T. Farrar, A. J. Plueddemann, and S. F. Zippel, 2023: Langmuir Turbulence Controls on Observed Diurnal Warm Layer Depths. *Geophysical Research Letters*, **50 (10)**, e2023GL103 231, https://doi.org/10.1029/2023GL103231.

Wijesekera, H. W., D. W. Wang, and E. Jarosz, 2020: Dynamics of the Diurnal Warm Layer: Surface Jet, High-Frequency Internal Waves, and Mixing. *J. Phys. Oceanogr.*, **50 (7)**, 2053–2070, https://doi.org/10.1175/JPO-D-19-0285.1.

Yu, C., J. Song, S. Li, and S. Li, 2022: On an Improved Second-Moment Closure Model for Langmuir Turbulence Conditions and Its Application. *J. Geophys. Res. Oceans*, **127 (5)**, e2021JC018 217, https://doi.org/10.1029/2021JC018217.